



Intervertebral disc segmentation in MR images using anisotropic oriented flux

Max W.K. Law^{a,b,*}, KengYeow Tay^{b,c}, Andrew Leung^{b,c}, Gregory J. Garvin^{b,d}, Shuo Li^{a,b}

^aGE Healthcare Canada, 268 Grosvenor Street, London, Ontario, Canada N6A 4V2

^bUniversity of Western Ontario, 1151 Richmond Street, London, Ontario, Canada N6A 3K7

^cLondon Health Sciences Centre, 800 Commissioners Road East, London, Ontario, Canada N6C 2R6

^dSt. Joseph's Health Care London, 268 Grosvenor Street, London, Ontario, Canada N6A 4V2

ARTICLE INFO

Article history:

Received 19 July 2011

Received in revised form 18 June 2012

Accepted 18 June 2012

Available online 23 July 2012

Keywords:

Spine

Intervertebral disc

Segmentation

Magnetic resonance images

Anisotropic oriented flux

ABSTRACT

This study proposes an unsupervised intervertebral disc segmentation system based on middle sagittal spine MR scans. The proposed system employs the novel anisotropic oriented flux detection scheme which helps distinguish the discs from the neighboring structures with similar intensity, recognize ambiguous disc boundaries, and handle the shape and intensity variation of the discs. Based on minimal user interaction, the proposed system begins with vertebral body tracking to infer the information regarding the positions and orientations of the target intervertebral discs. The information is employed in a set of image descriptors, which jointly constitute an energy functional describing the desired disc segmentation result. The energy functional is minimized by a level set based active contour model to perform disc segmentation. The proposed segmentation system is evaluated using a database consisting of 455 intervertebral discs extracted from 69 middle sagittal slices. It is demonstrated that the proposed method is capable of delivering accurate results for intervertebral disc segmentation.

© 2012 Elsevier B.V. All rights reserved.

1. Introduction

Intervertebral discs are spine components interposed between each pair of adjacent vertebrae. They are deformable and act as a buffer to allow vertebral movement. Disc degeneration can trigger various problems such as back pain, neck pain, numbness, tingling, loss of muscle strength, walking and standing difficulty and paralysis. There is vastly growing demand for tools to diagnose disorders. As one of the non-invasive diagnostic techniques, spinal magnetic resonance (MR) imaging is widely employed for diagnosis of intervertebral disc abnormalities. Manual disc assessment is time consuming. A system offering an accurate delineation of discs can greatly facilitate diagnosis. For instance, quantifying temporal changes of disc degeneration and herniation, evaluating disc hydration conditions based on the intensity inside segmented discs, estimating the dimensions of abnormal discs and their influence on the neighboring soft tissue.

Developing an algorithm to locate or segment the discs in MR images is extremely challenging. This is mainly due to the intensity resemblance between discs and their neighboring structures (Fig. 1a), ambiguous disc boundaries (Fig. 1b), a great variety of disc shapes (Fig. 1d) and inconsistent intensity patterns (Fig. 1e). In different image modalities, varying intensity inside the same spinal component adjacent to the discs also interferes with disc

boundary detection (see Fig. 2, at the posterior side of the discs, the bright cerebrospinal fluid and dark spinal nerves in Fig. 2a versus the grey cerebrospinal fluid and spinal nerves in Fig. 2b). They prevent conventional image segmentation techniques (Caselles et al., 1997; Xu and Prince, 1998; Vasilevskiy and Siddiqi, 2002) from delivering satisfactory disc segmentation results.

Most studies concerning image based intervertebral disc analysis are developed for disc labeling or locating disc centers without delineating the disc boundaries. Weiss et al. introduced an intensity thresholding based disc labeling system for sagittal spinal MR images (Weiss et al., 2006). Schmidt et al. proposed a supervised probabilistic model (Schmidt et al., 2007) which considers both intensity and geometric information for disc labeling. Corso et al. suggested enforcing an inter-disc distance constraint to improve the disc labeling accuracy (Corso et al., 2008). A disc orientation estimation scheme is also proposed (Abufadel et al., 2006) to automate the transverse imaging planning process. Considering spine anatomical information, Štern et al. (2010) devised an image gradient based algorithm to extract spine centerlines, and subsequently locate vertebrae and discs. Spine centerline detection results, along with disc template matching are employed for vertebra segmentation and disc labeling (Peng et al., 2005).

Only a limited number of approaches have addressed the challenging disc segmentation problem. Chevrefils et al. suggested a watershed segmentation algorithm (Chevrefils et al., 2007). Nonetheless, the watershed based algorithm persistently encounters an over-segmentation issue. To exploit the directional image features, a hough transform based approach was presented by Shi et al.

* Corresponding author at: University of Western Ontario, London, Ontario, Canada.

E-mail address: max.w.k.law@gmail.com (M.W.K. Law).

jointly constitute an energy functional which reflects the segmentation quality of a disc. Active contour disc segmentation is performed by a level set based minimization of the energy functional. These are explained in Section 4. A summary of the two-phase disc segmentation system is presented in Section 5.

The proposed segmentation system is validated using a dataset comprising 69 spine middle sagittal slices. These slices are extracted from 22 T2 and 11 PD spine sagittal MR sequences which were acquired from 22 subjects. There is a total of 455 2D intervertebral discs in different midsagittal slices. The experiment settings, results and discussion are presented in Section 6. The proposed system is shown to consistently achieve outstanding segmentation accuracies. Finally, Section 7 concludes this study.

2. Anisotropic oriented flux

The anisotropic oriented flux is a detection scheme which involves a set of linear image filters formulated in the Fourier domain. This scheme aims at capturing low level image features for detecting structures in 2D slices which intersect the target objects perpendicularly and are extracted from a volumetric image. The low level image features allow the construction of three different measures. These measures are employed in both phases of the segmentation system to help the detection of vertebral body regions (in the first phase) and disc-annuli (in the second phase).

The anisotropic oriented flux detection scheme is designed with five objectives in mind:

- detection of boundaries located at arbitrary distances away from a reference voxel to handle different structure sizes;
- insensitivity to the disturbance introduced by closely located objects;
- sensitivity to low contrast object boundaries;
- orientation sensitivity to capture directional spine intensity patterns;
- robustness against significant local intensity fluctuation inside the target structures (see the intensity profiles of the discs and the vertebral bodies in Fig. 2a).

It is noted that the widely employed linear heat equation based multi-scale techniques (Lowe, 2004; Lindeberg, 1998; Sato et al., 1998; Marr and Hildreth, 1980) are inappropriate for the second and the third objectives. It is because these techniques involve strong smoothing which annihilates blurry edges and small separations between closely located objects. Furthermore, the non-linear diffusion based schemes (Perona and Malik, 1990; Okada et al., 2004; Manniesing et al., 2006) depend on an accurate local orientation estimation to properly drive the anisotropic diffusion processes. They are possibly prone to the significant local intensity fluctuation.

To construct a low level feature extraction scheme for the aforementioned objectives, we aggregate the intensity changes occurring along the radial direction at an arbitrary distance from a local position using two complementary representations,

$$\frac{1}{4\pi r^2} \int_{\delta C_r} (\vec{\nabla} \cdot I)(\vec{x} + r\hat{n}) \cdot \hat{n} dA, \quad (1)$$

$$\frac{1}{4\pi r^2} \int_{\delta C_r} (\vec{\nabla} \cdot I)(\vec{x} + r\hat{n}) dA, \quad (2)$$

where C_r is a sphere with radius r , I is an image, \hat{n} and dA are respectively the outward normal and infinitesimal area on δC_r . These measures are scale invariant because of the surface area-normalization. The former quantifies if the intensity immediately inside the sphere surface is higher than that in the vicinity of the sphere. If r is the distance from \vec{x} to the closest object boundary, this measure encodes the intensity contrast between the object and its vicinity. On the other

hand, the magnitude of the latter captures the consistency of the image gradient on the sphere surface. When r is small, it helps detect an object boundary where the gradients within a local region of the boundary are pointing across the boundary.

They consider only the intensity changes occurring at the positions r away from \vec{x} . They are therefore capable of detecting distant object boundary and simultaneously avoid including closely located irrelevant objects outside C_r . They can detect blurry boundaries because they involve no strong smoothing in the calculation. In the following sub-sections, two orientation sensitive variants of the above measures are presented by realizing the relation between Eq. (1) and the published works (Vasilevskiy and Siddiqi, 2002; Law and Chung, 2009), and between Eq. (2) and the idea in Law and Chung (2010). The anisotropic oriented flux detection scheme is developed based on these orientation sensitive variants to cope with the intensity fluctuation when detecting 2D objects in the slices extracted from a volume.

2.1. Previous work

Eq. (1) is tangential to the gradient flux measure (Vasilevskiy and Siddiqi, 2002; Law and Chung, 2009) where a slight Gaussian pre-smoothing is applied to better handle local intensity fluctuation. Along the same research line, the orientation sensitive variant was proposed in Law and Chung (2008). It analyzes the image gradient after being projected along one specific direction distributed on the sphere surface. The orientation sensitive detection is preferred over the isotropic gradient flux operation for the analysis of objects which exhibit a directional intensity pattern, such as spinal image analysis. The oriented flux measured at a 3D position \vec{x} , along an arbitrary direction $\hat{\rho}$ is defined as,

$$f(\vec{x}; r, \hat{\rho}) = \frac{1}{4\pi r^2} \int_{\delta C_r} \left((\hat{\rho} \cdot \vec{\nabla} g * I(\vec{x} + r\hat{n})) \hat{\rho} \right) \cdot \hat{n} dA, \quad (3)$$

where g is a Gaussian function with a scale factor of 1 voxel-length, I is a volumetric image and $*$ is the convolution operator. This is an orientation sensitive version of Eq. (1). The best detection direction is the axis along which the oriented flux yields the maximum magnitude,

$$\hat{\rho}(\vec{x}; r) = \arg \max_{\hat{\rho}} |f(\vec{x}; r, \hat{\rho})|, \quad (4)$$

and based on the best detection direction, the detection response is,

$$f(\vec{x}; r, \hat{\rho}(\vec{x}; r)).$$

On the other hand, the orientation sensitive variant of Eq. (2) quantifies the image gradient consistency along an arbitrary direction $\hat{\rho}$ on the sphere surface for boundary detection (Law and Chung, 2010),

$$s(\vec{x}; r, \hat{\rho}) = \frac{1}{4\pi r^2} \int_{\delta C_r} \left(\hat{\rho} \cdot \vec{\nabla} I(\vec{x} + r\hat{n}) \right) dA. \quad (5)$$

2.2. The formulation

The optimal direction (Eq. (13)) computed in a volumetric image using the analytical formulation (Law and Chung, 2008; Law and Chung, 2010) can be any 3D direction. It is undesired when dealing with the analysis concerning individual image planes instead of the entire volumetric image. This includes the applications where the desired image planes are obtained during acquisition or synthesized upon the analysis, such as short-axis or long-axis cardiac image analysis, feature extraction on vessel cross-sectional plane for vascular tracking and sagittal spinal scan analysis. The voxel intensity inside the target objects can notably fluctuate, whereas there is a strong structural correspondence across the

adjacent image planes, at the same in-plane position. When the detection axis $\hat{\rho}$ lies on the desired image planes, the across-plane structural correspondence is naturally considered to help sustain the within-structure intensity fluctuation during the detection.

First, by applying divergence theorem on Eq. (3),

$$\frac{1}{4\pi r^2} \left(\int_{C_r} (\mathbf{g} * I)_{\hat{\rho}\hat{\rho}}(\vec{x} + \vec{v}) dV \right),$$

where dV is the infinitesimal volume in the sphere C_r . If $\hat{\rho}$ is a vector lying on a 2D plane which is defined by two orthogonal directions \hat{j}_1 and \hat{j}_2 , i.e. $\hat{\rho} = \hat{\rho}^T [\hat{j}_1 \ \hat{j}_2] \begin{bmatrix} \hat{j}_1^T \\ \hat{j}_2^T \end{bmatrix}$. As such, the above equation is equivalent to

$$\frac{1}{4\pi r^2} \int_{C_r} \left(\hat{\rho}^T [\hat{j}_1 \ \hat{j}_2] \begin{bmatrix} \mathbf{g}_{j_1 j_1} & \mathbf{g}_{j_1 j_2} \\ \mathbf{g}_{j_1 j_2} & \mathbf{g}_{j_2 j_2} \end{bmatrix} \begin{bmatrix} \hat{j}_1^T \\ \hat{j}_2^T \end{bmatrix} \hat{\rho} \right) * I(\vec{x} + \vec{v}) dV. \quad (6)$$

In the above equation, the derivatives are computed solely along the in-plane directions. It suppresses the across-plane intensity changes because of the across-plane structure consistency assumption. It is therefore most sensitive to the boundaries perpendicular to the slice. Nonetheless, the spherical formulation can detect a structure boundary slightly tilted along the across-slice direction in a less sensitive manner. It is flexible enough to handle target objects which passes obliquely across different slices. In addition, the isotropic smoothing operation in the above equation is replaced by an anisotropic variant to enforce a stronger smoothing along the across-plane direction than along the in-plane directions. This anisotropic smoothing allows the algorithm to capture the structural consistency at the same in-plane positions but across adjacent slices. Denote $h(\vec{x}; \hat{\rho}, \sigma)$ is a three dimensional function which is Gaussian along $\hat{\rho}$ and constant along other dimensions,

$$h^{\hat{\rho}, \sigma}(\vec{x}) = \frac{1}{\sqrt{2\pi}\sigma} \exp\left(-\frac{(\vec{x} \cdot \hat{\rho})^2}{2\sigma^2}\right). \quad (7)$$

To introduce anisotropic smoothing to Eq. (6), the Gaussian function g is decomposed into three Gaussian functions $h(\cdot)$, with a scale parameter σ_j for the in-plane directions and another scale parameter σ_a for the across-plane direction. To facilitate the discussion, we regard convolving a matrix function with a scalar function as convolving each entry of the matrix function with the scalar function, and results in a matrix function. Eq. (6) becomes

$$\hat{\rho}^T [\hat{j}_1 \ \hat{j}_2] \left(\frac{1}{4\pi r^2} \int_{C_r} \begin{bmatrix} (h^{\hat{j}_1, \sigma_j} * h^{\hat{j}_2, \sigma_j})_{j_1 j_1} & (h^{\hat{j}_1, \sigma_j} * h^{\hat{j}_2, \sigma_j})_{j_1 j_2} \\ (h^{\hat{j}_1, \sigma_j} * h^{\hat{j}_2, \sigma_j})_{j_1 j_2} & (h^{\hat{j}_1, \sigma_j} * h^{\hat{j}_2, \sigma_j})_{j_2 j_2} \end{bmatrix} * h^{(\hat{j}_1, \hat{j}_2), \sigma_a} * I(\vec{x} + \vec{v}) dV \right) [\hat{j}_1 \ \hat{j}_2]^T \hat{\rho}. \quad (8)$$

The anisotropic Gaussian smoothing is applied to Eq. (5) in a similar fashion and $s(\cdot)$ becomes

$$\hat{\rho}^T [\hat{j}_1 \ \hat{j}_2] \left(\frac{1}{4\pi r^2} \int_{C_r} \begin{bmatrix} (h^{\hat{j}_1, \sigma_j} * h^{\hat{j}_2, \sigma_j})_{j_1} \\ (h^{\hat{j}_1, \sigma_j} * h^{\hat{j}_2, \sigma_j})_{j_2} \end{bmatrix} * h^{(\hat{j}_1, \hat{j}_2), \sigma_a} * I(\vec{x} + \vec{v}) dV \right). \quad (9)$$

The integrals in the above equations are converted to convolution operations (Law and Chung, 2009). As such, Eqs. (8) and (9) are expressed in the form of,

$$\hat{\rho}^T [\hat{j}_1 \ \hat{j}_2] (\psi * I(\vec{x}; r)) [\hat{j}_1 \ \hat{j}_2]^T \hat{\rho}, \quad (10)$$

$$\hat{\rho}^T [\hat{j}_1 \ \hat{j}_2] (\vec{\phi} * I(\vec{x}; r)), \quad (11)$$

respectively. These two measures are referred to as *anisotropic gradient flux* and *anisotropic gradient consistency* respectively. Here

$\psi(\vec{x}; r)$ is a 2×2 matrix function, and thus the filtering response $\psi * I(\vec{x}; r)$ for each combination of \vec{x} and r is a 2×2 matrix. Meanwhile, $\vec{\phi}(\vec{x}; r)$ is a 2D vector function, of which the response $\vec{\phi} * I(\vec{x}; r)$ is a 2D vector for each combination of \vec{x} and r . Based on Hankel transforms (Bracewell, 1986), the analytical formulation of $\psi(\vec{x}; r)$ and $\vec{\phi}(\vec{x}; r)$ are obtained in the Fourier domain,

$$\begin{aligned} \Psi(\vec{u}; r) &= [\hat{j}_1 \ \hat{j}_2]^T (\vec{u} \vec{u}^T) [\hat{j}_1 \ \hat{j}_2] \left(\frac{2r \cos(r|\vec{u}|)}{|\vec{u}|^2} - \frac{4\pi \sin(r|\vec{u}|)}{|\vec{u}|^3} \right) \\ &\quad \times \exp \left\{ -\frac{1}{2} ((\sigma_j |\hat{j}_1 \hat{j}_2^T \vec{u}|)^2 + \sigma_a (\hat{j}_1 \times \hat{j}_2 \cdot \vec{u})^2) \right\}, \\ \vec{\Phi}(\vec{u}; r) &= \frac{\sqrt{-1} (\hat{j}_1 \ \hat{j}_2)^T \vec{u} \sin(r|\vec{u}|)}{r|\vec{u}|} \\ &\quad \times \exp \left\{ -\frac{1}{2} ((\sigma_j |\hat{j}_1 \hat{j}_2^T \vec{u}|)^2 + \sigma_a (\hat{j}_1 \times \hat{j}_2 \cdot \vec{u})^2) \right\}, \end{aligned} \quad (12)$$

where \vec{u} is the angular frequency in radian per physical length (mm in this study).

There are three independent channels in the symmetric 2×2 matrix function $\Psi(\cdot)$ and two independent channels in the 2D vector function $\vec{\Phi}(\cdot)$. The purpose of anisotropic gradient consistency (Eq. (11)) is to measure the consistency of image gradient on the detection sphere surface. It is useful to capture an object boundary by identifying the consistent gradient in a small local region around an intensity edge. On the other hand, anisotropic gradient flux (Eq. (10)) quantifies the amount of gradients after being projected along $\hat{\rho}$, pointing in or out from C_r . Fig. 3a illustrates a normalized gradient pattern on the sphere surface δC_r that induces a large value of $\hat{\rho}^T [\hat{j}_1 \ \hat{j}_2] (\psi * I(\vec{x}; r)) [\hat{j}_1 \ \hat{j}_2]^T \hat{\rho}$. The magnitude of this measure briefly indicates the intensity difference between the local region defined by C_r and its vicinity in the direction of $\pm \hat{\rho}$. Its sign reveals if the local region has stronger intensity than its vicinity along the axis $\pm \hat{\rho}$ does. The most representative direction for evaluating the anisotropic gradient flux is obtained as,

$$[\hat{j}_1 \ \hat{j}_2]^T \left(\arg \max_{\hat{\omega}} |\hat{\omega}^T [\hat{j}_1 \ \hat{j}_2] (\psi * I(\vec{x}; r)) [\hat{j}_1 \ \hat{j}_2]^T \hat{\omega}| \right). \quad (13)$$

The maximization with respect to the 2D projection axis $\hat{\omega}$ is achieved by acquiring the eigenvector of the matrix $[\hat{j}_1 \ \hat{j}_2] (\psi * I(\vec{x}; r)) [\hat{j}_1 \ \hat{j}_2]^T$ corresponding to the eigenvalue having the largest magnitude.

To this end, the anisotropic oriented flux offers three different measures which are employed in our disc segmentation system,

- Anisotropic gradient flux measure, Eq. (10);
- Anisotropic gradient consistency measure, Eq. (11);
- The most representative detection direction of the anisotropic gradient flux measure, Eq. (13).

Unless specified, the anisotropic smoothing strength of ψ and $\vec{\phi}$, σ_j (for in-plane direction) and σ_a (for axial direction) are fixed to be l and $2l$ respectively in this paper where l is the in-plane voxel-length.

As a summary of the anisotropic oriented flux formulation, the anisotropic gradient flux measure and anisotropic gradient consistency measure are tailored to only recognize intensity changes occurring along the in-plane directions. Their detection directions ($\hat{\rho}$ in Eqs. (6)–(11)) and the resultant optimal direction (Eq. (13)) are specified to be in-plane directions. Meanwhile, the intensity changes taking place across planes is omitted based on the assumption that the image planes perpendicularly intersect the interested objects and the structure discrepancy across adjacent planes at the same in-plane position is unimportant. This assumption is further exploited by introducing anisotropic Gaussian smoothing to capture the across-plane structure consistency.

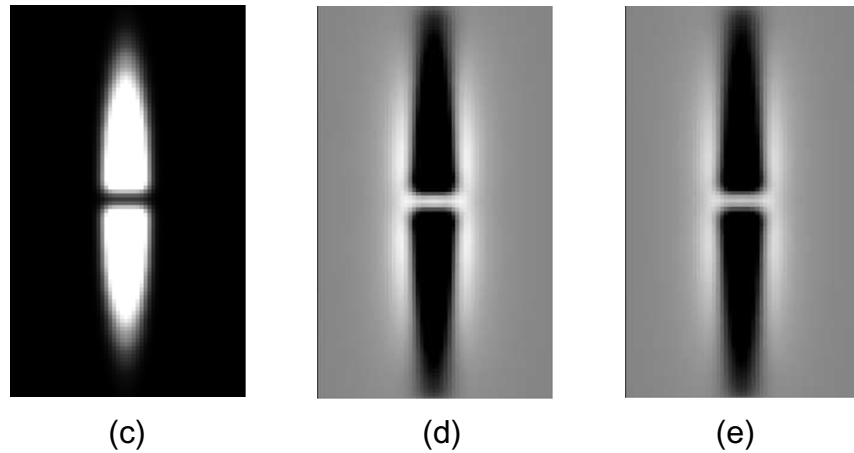
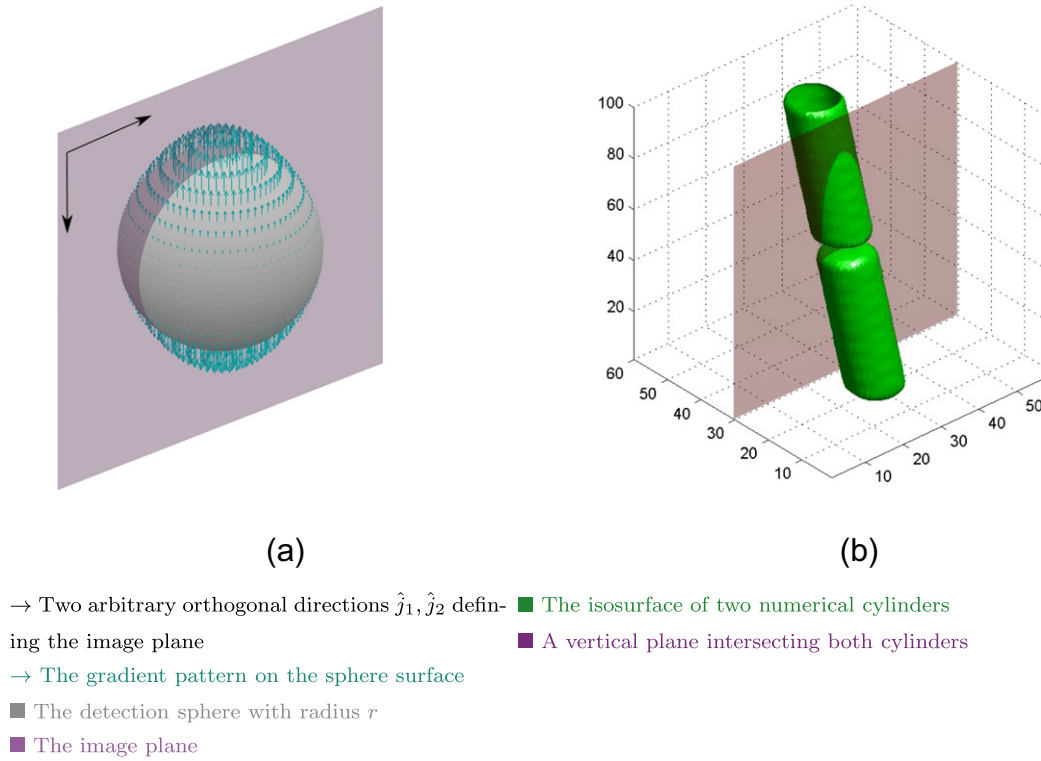


Fig. 3. (a) The gradient pattern has a unit sum of L_2 -norm on the detection sphere surface. This gradient pattern produces the maximum response from Eq. (10) when $\hat{\rho}$ is the vertical direction. (b) Two 3D synthetic cylinders, intensity value is 1 inside the cylinders and 0 elsewhere. (c) The intensity at the image plane shown in (b). (d) The anisotropic oriented flux measure $V_l(\vec{x})$ observed at the plane shown in (b). (e) The same anisotropic oriented flux measure as (d) after the vertical image plane is replaced by an all-zero plane.

3. Coarse vertebral body detection

Based on the aforementioned measures, this section devises a detection scheme for the first phrase of the disc segmentation system – coarse detection of vertebral body regions. The coarse detection is an iterative procedure which progressively tracks each vertebral body along the spine. Each iteration makes use of two pieces of information returned by its predecessor – the tracking direction (an approximated direction from the center of the superior endplate to the center of the inferior endplate) and the tracking position (an arbitrary position inside the currently tracking vertebral body). They are manually supplied for the first vertebral body by two user selected positions, the position (\vec{z}_1) of the vertebra immediately underneath the top target disc and that (\vec{z}) underneath the bottom target disc. They indicate the first vertebra and

the last vertebra, and also jointly define the initial tracking direction $\hat{q}_0 = \frac{\vec{z} - \vec{z}_1}{|\vec{z} - \vec{z}_1|}$. The algorithm iteratively discovers each vertebral body and calibrates the spine tracking direction (\hat{q}_i for the i th vertebral body), until reaching the vertebral body containing the second selected position. The main idea of the coarse detection phase is to estimate the statistics (Fig. 8) required by the subsequent disc segmentation phase. It is noted that a precise delineation of the vertebra boundary is not the focus of this study. In the clinical environment, accurate vertebral boundary detection is based on computed tomographic (CT) images. Readers are referred to Nyul et al. (2005), Štern et al. (2010), and Kadoury and Paragios (2010) for the details regarding spine CT image analysis approaches.

The technical challenges of the vertebral body region detection are the significant intensity fluctuations induced by the bone marrow inside vertebrae, the nearby spinal cord and disc-nuclei which

have high intensity. The anisotropic gradient flux measure is applied with consideration of the tracking direction, to emphasize the high intensity regions interposed between two local intensity regions along the spine tracking direction. This focuses on recognizing the top and bottom boundaries of the vertebra, while it is robust against the disturbance introduced by the high intensity spinal cord. Additional image smoothing is utilized to suppress the undesired local intensity fluctuation. This formulation returns filtering responses in the entire slice sequence. The response in each interested sagittal slice is zero-thresholded to give a set of 2D binary regions. These 2D binary regions are processed by a new morphological operation *Maximum directional distance transform*, followed by a connectivity analysis to obtain the coarse detection of the vertebral body. The vertebra statistics are finally extracted from the detected region in the first phase of the proposed segmentation system.

3.1. Anisotropic gradient flux for vertebral body detection

In sagittal T2 and PD MR images, the bright vertebral bodies are surrounded by two different types of dark and elongated structures – the disc-annuli beyond the superior and inferior endplates, and the ligaments outside the anterior and posterior boundaries. The disc-annuli separate a vertebral body from its adjacent counterparts and the adjacent disc-nuclei, which share a similar intensity range as the vertebrae. On the other hand, beyond the ligaments, structures such as the spinal cord and abdominal vessels exhibit a much more diverse intensity range than the vertebrae. In the vicinity of the vertebral bodies, such a diverse intensity range creates inconsistent intensity patterns. They are problematic when detecting the vertebral body based on the anterior and posterior boundaries. Therefore, 2 different descriptors are employed; one to detect the vertebrae based on the superior and inferior boundaries, the other based on the anterior and posterior boundaries which possess more diverse intensity patterns immediately outside the boundaries.

As discussed in Section 2, a negative response from Eq. (10) represents a high intensity region interposing between two low intensity regions along the axis $\pm\hat{\rho}$. To detect a bright vertebral body interposed between two low intensity disc-annuli, the term $\hat{\rho}$ in Eq. (10) is replaced by the vertebral body tracking direction. This direction is approximated by the tracking direction of the previously tracked vertebral body \hat{q}_{i-1} . For the i th vertebral body, based on the intensity changes occurring across the vertebra endplates, the vertebral body is highlighted by,

$$\hat{q}_{i-1}^T [\hat{j}_1 \hat{j}_2] (\psi * I(\vec{x}; r)) [\hat{j}_1 \hat{j}_2]^T \hat{q}_{i-1}. \quad (14)$$

The distance between a reference voxel and the closest vertebra endplates is obtained using the strongest-over-radii strategy,

$$r_a(\vec{x}) = \arg \max_{r \in \mathbb{R}_h} \left| \hat{q}_{i-1}^T [\hat{j}_1 \hat{j}_2] (\psi * I(\vec{x}; r)) [\hat{j}_1 \hat{j}_2]^T \hat{q}_{i-1} \right|. \quad (15)$$

It searches for the most significant intensity change which corresponds to an object boundary, within a set of detection radii defined in \mathbb{R}_h . This radius set has one radius sample for each in-plane pixel length l and covers the radii ranged from l to half of the largest detectable vertebral body height (defined as 50 mm in this study). The gradient at the vertebra endplate is generally aligned along the spine tracking direction and points into the bright vertebral body regions. Based on Eq. (10), this is reflected by a negative response from the following equation,

$$V_{d,i}(\vec{x}) = \hat{q}_{i-1}^T [\hat{j}_1 \hat{j}_2] (\psi * I(\vec{x}; r_a(\vec{x}))) [\hat{j}_1 \hat{j}_2]^T \hat{q}_{i-1}. \quad (16)$$

This descriptor gives the strongest response at locations near to the center of a vertebral body. At these locations, both detection sphere

poles (see Fig. 3 where the gradient arrows are longest at the sphere poles) reach the superior and the inferior vertebral endplates which simultaneously contribute to a negative detection response. The above descriptor returns a weaker negative response when \vec{x} approaches either the superior endplate or the inferior endplate of the vertebra. It is because the response is induced from only one contact region between the detection sphere and an endplate. On the other hand, inside the disc-annulus immediately beyond a vertebral endplate, a positive response is observed as the gradient which is pointing away from the low intensity disc-annulus into the adjacent high intensity vertebral body. When \vec{x} drifts away from the horizontal center of a vertebral body along the anterior–posterior axis, the contact area between the detection sphere poles and the vertebral endplates shrinks. The detection response $V_{d,i}(\cdot)$ is weakened and is vulnerable to intensity changes occurring outside the vertebra.

Vertebral body detection based on the anterior and posterior vertebral boundaries is more challenging. The intensity patterns in the vicinity of these boundaries are inconsistent. In addition, the boundary orientations at the corners of the vertebral body can be diverse. Therefore, it is beneficial to simultaneously search for the best detection direction and the best detection sphere radius to identify the most significant object boundaries. It is noted that the best detection direction searches (see Eq. (13)) can bias towards the bone marrow induced local intensity fluctuation for small detection radii. The detection responses obtained according to the biased direction can be unfavorably boosted. As such, the search of the best detection direction for an arbitrary radius involves an additional Gaussian smoothing to suppress the local intensity fluctuation,

$$\arg \max_{\hat{\omega}} \left| \hat{\omega}^T [\hat{j}_1 \hat{j}_2] (g * \psi * I(\vec{x}; r)) [\hat{j}_1 \hat{j}_2]^T \hat{\omega} \right|. \quad (17)$$

Here the Gaussian smoothing can be embedded in the anisotropic gradient flux by specifying a different set of smoothing strength,

$$\hat{\omega}(\vec{x}; r) = \arg \max_{\hat{\omega}} \left| \hat{\omega}^T [\hat{j}_1 \hat{j}_2] (\psi^{\sigma_j=2l, \sigma_a=3l} * I(\vec{x}; r)) [\hat{j}_1 \hat{j}_2]^T \hat{\omega} \right|. \quad (18)$$

The strongest-over-radii technique similar to Eq. (15) is applied to find the best detection radius based on the detected detection direction,

$$r_b(\vec{x}) = \arg \max_{r \in \mathbb{R}_t} \left| \hat{\omega}^T(\vec{x}; r) [\hat{j}_1 \hat{j}_2] (\psi * I(\vec{x}; r)) [\hat{j}_1 \hat{j}_2]^T \hat{\omega}(\vec{x}; r) \right|. \quad (19)$$

The radius set \mathbb{R}_t is different from \mathbb{R}_h in Eq. (15). It is comprised of the radius samples ranged from l to R_t for one sample per unit pixel-length. R_t is suggested to be the half of the thickness of the thinnest detectable disc. An undersized R_t causes over-sensitivity to local intensity fluctuation while with an exceeding value of R_t , the system possibly omits small desired structures. Searching the detection radius within the smaller radius set \mathbb{R}_t can suppress false positive detection induced by the inconsistent intensity patterns outside the vertebral body boundaries. It is noted that the extra smoothing is applied only for evaluating $\hat{\omega}(\vec{x}; r)$ to provide a more reliable detection direction estimation. During the strongest-over-radii search, it is omitted to avoid extending the effective coverage of $\psi(\cdot)$. Detection based on the extended coverage can include unexpected neighboring objects farther than the maximum radius of \mathbb{R}_t . The descriptor based on $r_b(\vec{x})$ is

$$V_l(\vec{x}) = \hat{\omega}^T(\vec{x}; r_b(\vec{x})) [\hat{j}_1 \hat{j}_2] (\psi * I(\vec{x}; r_b(\vec{x}))) [\hat{j}_1 \hat{j}_2]^T \hat{\omega}(\vec{x}; r_b(\vec{x})) \quad (20)$$

Prior to further elaboration of vertebral body detection, the above descriptor is employed to illustrate the advantage of the proposed approach which applies 3D anisotropic oriented flux measures to detecting 2D structures in the image planes embedded in a volume. This discussion focuses on a vertical plane embedded in a numerical

volume consist of two cylinders (Fig. 3b). The voxel intensity and the response $V_i(\vec{x})$ on this plane are illustrated in Fig. 3c and d respectively. To exaggerate the condition where low intensity reduces local image contrast, the vertical image plane in Fig. 3b and c is replaced by an all-zero image plane. This all-zero plane supplies no intensity contrast. Nonetheless, the descriptor based on 3D anisotropic oriented flux is capable of delivering promising responses (Fig. 3e) by factoring in the neighboring slice intensity. The anisotropic oriented flux exploits across-plane consistency to deal with low contrast structures. Furthermore, the abrupt intensity changes between the all-zero plane and its adjacent image planes have no impact on the estimation of the most representative detection direction of the anisotropic oriented flux. It is because the direction estimation is operated along the image plane and omits the across-plane intensity fluctuation. Therefore, 3D anisotropic oriented flux based measures obtained at individual 2D image planes offer promising robustness against low contrast objects. They convey reliable image features for detection and segmentation of 2D structures in the image slices embedded in a volume.

To this end, there are two different descriptors $V_{d,i}(\vec{x})$ and $V_i(\vec{x})$ (Eqs. (16) and (20)) for the coarse vertebral body detection. The former is tracking direction-dependent and focuses on the superior–inferior axis of the vertebra with the help of the tracking direction \hat{q}_{i-1} . It senses the intensity changes across the vertebra endplates. Within a relatively smaller searching region, the latter is general for all vertebral body and recognizes all types of intensity changes including the intensity changes across the vertebral body anterior and posterior boundaries. Grounded on the scale-invariant anisotropic oriented flux analysis, these descriptors report a negative response when the local intensity is generally higher than the vicinity. They are competed to form a final descriptor which emphasizes the vertebral body regions,

$$V_i(\vec{x}) = \begin{cases} V_{d,i}(\vec{x}) & \text{if } |V_{d,i}(\vec{x})| \geq |V_i(\vec{x})|, \\ V_i(\vec{x}) & \text{otherwise.} \end{cases} \quad (21)$$

In general, the regions having stronger intensity than their vicinity induce negative $V_i(\cdot)$. In particular, $V_i(\cdot)$ is more sensitive to the intensity changes taking place along the tracking direction \hat{q}_{i-1} because of the term $V_{d,i}(\cdot)$. Immediately beyond the boundary of these high intensity regions, there are positive valued $V_i(\cdot)$ areas. Fig. 4a–c depict an original spine image, the response image and the negative response region. Based on this detection response, a zero-thresholding capturing negative regions of $V_i(\cdot)$ can include the target vertebral body in the detection results. The target regions are analyzed as described in Sections 3.2 and 4, for the extraction of the vertebral statistics (Fig. 4d) and final disc segmentation contours (Fig. 4e).

Fig. 4f and g exemplify the responses obtained using the original optimally oriented flux (Law and Chung, 2008). Acquiring image gradient, so that the differential edge detection responses can be regarded as high-pass filtering that naturally amplifies image noise. Without the slice orientation-dependent anisotropic smoothing, the response image is notably more sensitive to local intensity fluctuation, particularly to those inside vertebral bodies (compare Fig. 4b against Fig. 4f). The associated thresholded regions shown in Fig. 4g are significantly more noisy and ill-suited to the task of vertebra tracking.

3.2. Maximum directional distance based region extraction

Subsequent to the thresholding of the detection response, connectivity analysis and a set of morphological operations are performed on each slice to distinguish the vertebral body regions from the irrelevant thresholded objects. The morphological operations aim at handling false-positive and false-negative pixels in the 2D thresholding results so that the target vertebral body regions

can be extracted as a connected component associated with the tracking point \hat{z}_i .

Due to the intensity fluctuation inside vertebral bodies and image noise, the response $V_i(\cdot)$ slightly fluctuates around zero at the positions where the neighboring object boundaries are significant compared to the local intensity fluctuation. The fluctuation leads to a considerable amount of false-positive and false-negative regions in the thresholded filtering response. A significant amount of false-positive pixels increases the chance where the vertebral body regions are unfavorably connected with irrelevant objects, while significant false-negative errors can split the detected vertebral body into multiple disjointed segments.

The false-positive and false-negative regions are caused by random intensity fluctuation. They are mostly narrow and have irregular shapes. The conventional morphological operations are employed to remove the narrow or small regions in a binary image. The description of the conventional morphological operations begins with the signed distance transform operator,

$$\mathcal{D}\{B(\vec{y})\}, \quad (22)$$

where \vec{y} is a coordinate in the 2D binary image $B(\cdot)$, the magnitude of $\mathcal{D}\{B(\vec{y})\}$ is the distance from \vec{y} to the closest object boundary, the signed distance is positive for the regions where $B(\vec{y}) = 0$ and vice versa. Denote $\mathcal{H}(\cdot)$ as the Heaviside function, which is 1 if the input argument is positive and 0 otherwise. The operations $\mathcal{H}(\mathcal{D}\{B(\vec{y})\} - d)$ and $\mathcal{H}(\mathcal{D}\{B(\vec{y})\} + d)$ are respectively equivalent to retreating and advancing the boundaries of the foreground objects in a distance of d . They are conventional *dilation* or *erosion* operations based on a circular structural element with a radius of d . Combinations of these two operations, the *closing* operation $\mathcal{H}(\mathcal{D}\{\mathcal{H}(\mathcal{D}\{B(\vec{y})\} - d)\} + d)$, and the *opening* operation $\mathcal{H}(\mathcal{D}\{\mathcal{H}(\mathcal{D}\{B(\vec{y})\} + d)\} - d)$ are capable of eliminating narrow or small background and foreground regions respectively.

Nonetheless, dilation can misidentify the straight and narrow background elements as a part of the foreground. These background elements can be crucial, for instance, the low intensity ligaments and disc-annuli which surround the vertebral bodies (Fig. 1a) are straight and narrow background regions in the thresholding result of $V_i(\cdot)$. On the other hand, erosion enlarges the irregular false-negative regions and can deteriorate the detection result. Here we introduce the directional distance transform to analyze the regularity of a region, and ultimately handle the false-negative and the false-positive errors. The directional distance transform is defined as,

$$\mathcal{D}\{B(\vec{y}); \hat{\omega}\}. \quad (23)$$

This operation is similar to $\mathcal{D}\{B(\vec{y})\}$ except that the closest boundary search is performed only along $\pm\hat{\omega}$. The resultant distance is ∞ if there is no boundary observed along $\pm\hat{\omega}$. As such,

$$\begin{aligned} \mathcal{D}\{B(\vec{y})\} &\equiv \mathcal{D}\{B(\vec{y}); \hat{\omega}^{\min}(\vec{y})\} \text{ where } \hat{\omega}^{\min}(\vec{y}) \\ &= \arg \min_{\hat{\omega}} |\mathcal{D}\{B(\vec{y}); \hat{\omega}\}|. \end{aligned} \quad (24)$$

Here we define the *Maximum directional distance transform*,

$$\mathcal{D}^{\max}\{B(\vec{y})\} = \mathcal{D}\{B(\vec{y}); \hat{\omega}^{\max}(\vec{y})\} \text{ where } \hat{\omega}^{\max}(\vec{y}) = \arg \max_{\hat{\omega}} |\mathcal{D}\{B(\vec{y}); \hat{\omega}\}|. \quad (25)$$

The practical impact of the maximum directional distance transform (Eq. (25)) is the capability of reporting huge distances in straight or low curvature narrow structures while it gives small distances in narrow and irregular regions. The narrow and irregular structures are therefore distinctive after the maximum directional distance transform is performed. Fig. 5a presents six objects in a binary image in which, three of them (left) are separated by a straight line and a low curvature line; two of them (middle) are

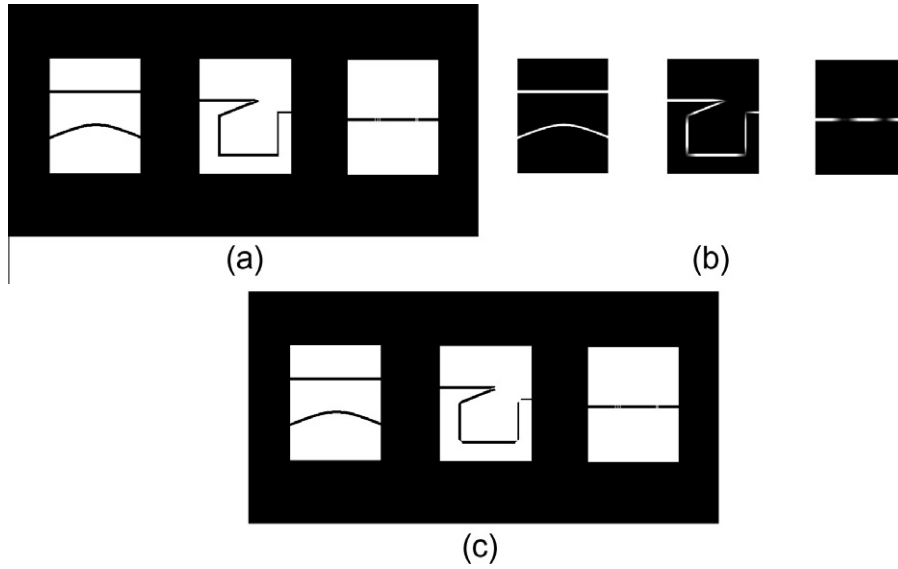


Fig. 5. (a) A binary image comprises of six white objects, where the width of the black horizontal straight lines is 6 pixel-length. (b) The maximum distance transform result of the binary image shown in (a). Black pixels represent non-positive signed distance values, white represent the values equal to or above 25. (c) The resultant binary image of Eq. (26), $d = 6$ pixel-length.

Algorithm 1. ConnectedTo[$B(\cdot), \vec{y}$]

Input: A binary image $B(\cdot)$ and position vector \vec{y} Output: A binary image containing one connected component ConnectedTo[$B(\cdot), \vec{y}$],

- 1: Perform connectivity analysis on the binary image $B(\cdot)$
- 2: **if** find a component connected to \vec{y} **then**
- 3: Return a binary image that is 1 for all member pixels in this component, 0 elsewhere.
- 4: **else**
- 5: For each component, compute the shortest distance from its member pixels to \vec{y}
- 6: Find the component having the minimum shortest distance to \vec{y} among all components
- 7: Return a binary image that is 1 for the member pixels in this component, 0 elsewhere.
- 8: **end if**

END

height of each region (see Fig. 8) are extracted based on a quadrangle fitting procedure described in A. The most suitable candidate (indexed as \tilde{m}_i for the i th vertebral body) is selected according to,

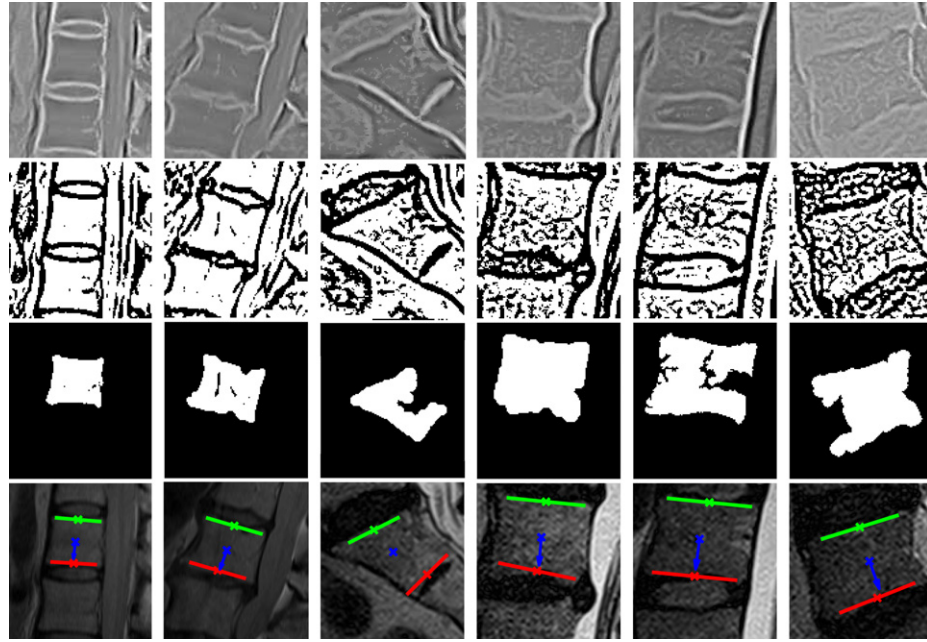
$$\tilde{m}_i = \begin{cases} \arg \min_{m \in \{1..6\}} \left(\frac{\max(v_{H,1}^{Output_m}, v_{W,1}^{Output_m})}{\min(v_{H,1}^{Output_m}, v_{W,1}^{Output_m})} \right) & \text{if } i = 1 \\ \arg \min_{m \in \{1..6\}} \left(\frac{\max(v_{W,i-1}, v_{W,i}^{Output_m})}{\min(v_{W,i-1}, v_{W,i}^{Output_m})} + \frac{\max(v_{H,i-1}, v_{H,i}^{Output_m})}{\min(v_{H,i-1}, v_{H,i}^{Output_m})} \right) & \text{otherwise.} \end{cases} \quad (27)$$

For the first vertebral body, the selected region is the candidate which resembles a square. While for the rest of the vertebral bodies, the widths and the heights of these candidates are compared against those from the immediate predecessors. The idea behind these criteria is eliminating the candidates which are connected to the region outside the vertebral body (mostly the spinal cord) as exemplified in Output₁ of Fig. 7, or the undersized regions (Output₂ or Output₄ in Fig. 7). These mis-connected and undersized candidates return a considerable dimension discrepancy to the normally detected vertebral bodies. On the other hand, different coarse detection results as shown in Output₃, Output₅ and Output₆ of Fig. 7 which give a decent estimation of the tracking direction, the

The aforementioned schemes result in six different detected vertebral bodies. Vertebral statistics including the width and the

Table 1
Four different schemes to complement the connectivity analysis for coarse detection of vertebral body regions as described in Algorithm 1.

		False-negative error	
		Negligible	Significant
<i>False-positive error</i>			
Negligible	Scheme-I Description: The vertebral body is recognized as one connected region which is disconnected from other irrelevant objects. Processing: No	Scheme-III Description: The vertebral body is recognized as multiple disjoint regions which are all disconnected from other irrelevant objects. Processing: Robust maximum directional distance based dilation	
	Scheme-II Description: The vertebral body is recognized as one connected region which is connected to other irrelevant objects. Processing: Conventional opening		
Significant	Scheme-IV Description: The vertebral body is recognized as multiple disjoint regions, some of which are connected to other irrelevant objects Processing: Robust maximum directional distance based dilation + Maximum directional distance based dilation		



x Region top-boundary center $\vec{v}_{TP,i}$ — Region width $v_{W,i}$, top-boundary direction $\pm \hat{v}_{TD,i}$
 x Region bottom-boundary center $\vec{v}_{BP,i}$ — Region width $v_{W,i}$, bottom-boundary direction $\pm \hat{v}_{BD,i}$
 x Region centroid: $\vec{v}_{C,i}$ → Tracking direction \hat{q}_i (Not available for the last vertebral body)

Fig. 6. The examples where the vertebral body region is extracted by one of the six refinement schemes. First row: The anisotropic gradient flux vertebral feature, $V_i(\cdot)$. Second row: The zero-thresholded feature, $\mathcal{H}(-V_i(\cdot))$. Third row: The extracted vertebral body regions according to the procedures described in Algorithm 1. From left to right, these sub-figures correspond to resultant regions $\text{Output}_1, \text{Output}_2, \dots, \text{Output}_6$ described in Algorithm 1. Fourth row, the overlay of the vertebra statistics and the original image.

top- and bottom-boundaries are acceptable for extracting vertebra statistics for disc segmentation.

4. Disc segmentation

The coarse detection of vertebral body region supplies the positions and orientations of the vertebra top- and bottom-boundaries for the second phase of the system, disc segmentation. Based on these positional and directional information of the adjacent vertebral bodies, a preliminary estimation of disc positions, sizes and orientations are conducted as described in B.

4.1. Anisotropic gradient flux and anisotropic gradient consistency for disc detection

The intensity range of discs (from low intensity disc-annuli to high intensity disc-nuclei) largely overlaps with those of their neighboring structures, such as ligaments, spinal cord, vertebral bodies and abdominal vessels. The intensity contrast at different sections of a disc boundary varies considerably. Therefore, disc segmentation requires a combination of multiple image descriptors to handle different conditions at various parts of a disc boundary. The segmentation algorithm is designed to,

- include the low intensity disc-annuli. The disc-annuli are interposed between two strong intensity structures presenting along the superior–inferior axis $\pm \hat{d}_{S,i}$. Based on the discussion of Eq. (11) in Section 2, such regions can be detected by a large value of,

$$D_{1,i}(\vec{x}; r) = (\hat{d}_{S,i})^T [\hat{j}_1 \ \hat{j}_2] (\psi * I(\vec{x}; r)) [\hat{j}_1 \ \hat{j}_2]^T \hat{d}_{S,i}. \quad (28)$$

- exclude the low intensity ligaments. In the sagittal MR scans, ligaments are narrow longitudinal structures located on the posterior side and the anterior side of each vertebral body. They are also

superficial to the discs (see Fig. 1a). They are low intensity structures interposed between the bright vertebral bodies and the bright fluid surrounding the spinal cord, or between the vertebral bodies and the irrelevant structures exhibiting low and fluctuating intensity. The ligaments above the disc are detected by,

$$\begin{aligned}
 D_{2,i}(\vec{x}; r) = & \overbrace{\mathcal{H}\left(\left(\vec{x} - \vec{v}_{BP,i-1}\right) \cdot \begin{bmatrix} \hat{j}_1 & \hat{j}_2 \\ 1 & 0 \end{bmatrix} \begin{bmatrix} \hat{j}_1 \\ \hat{j}_2 \end{bmatrix} \hat{v}_{BD,i-1}\right)}^{\text{Return 1 above the bottom-boundary of the superior vertebral body, 0 elsewhere}} \\
 & \times \left(\underbrace{(|(\vec{\phi} * I(\vec{x}; r)) \cdot \hat{v}_{BD,i-1}|)}_{\text{Detect the longitudinal edges exhibiting intensity changes along the directions } \pm \hat{v}_{BD,i-1}} \right) \\
 & + \left(\underbrace{(|(\hat{v}_{BD,i-1})^T (\psi * I(\vec{x}; r)) \hat{v}_{BD,i-1}|)}_{\text{Detect the longitudinal narrow areas which have an intensity different from that of the adjacent structures in the directions of } \pm \hat{v}_{BD,i-1}} \right) \quad (29)
 \end{aligned}$$

Analogously, the ligaments beneath the disc is detected by,

$$\begin{aligned}
 D_{3,i}(\vec{x}; r) = & \overbrace{\mathcal{H}\left(\left(\vec{x} - \vec{v}_{TP,i}\right) \cdot \begin{bmatrix} \hat{j}_1 & \hat{j}_2 \\ -1 & 0 \end{bmatrix} \begin{bmatrix} \hat{j}_1 \\ \hat{j}_2 \end{bmatrix} \hat{v}_{TD,i}\right)}^{\text{Return 1 below the top-boundary of the inferior vertebral body, 0 elsewhere}} \\
 & \times \left(\underbrace{(|(\vec{\phi} * I(\vec{x}; r)) \cdot \hat{v}_{TD,i}|)}_{\text{Detect the longitudinal edges exhibiting intensity changes along the directions } \pm \hat{v}_{TD,i}} \right) \\
 & + \left(\underbrace{(|(\hat{v}_{TD,i})^T (\psi * I(\vec{x}; r)) \hat{v}_{TD,i}|)}_{\text{Detect the longitudinal narrow areas which have an intensity different from that of the adjacent structures in the directions of } \pm \hat{v}_{TD,i}} \right) \quad (30)
 \end{aligned}$$

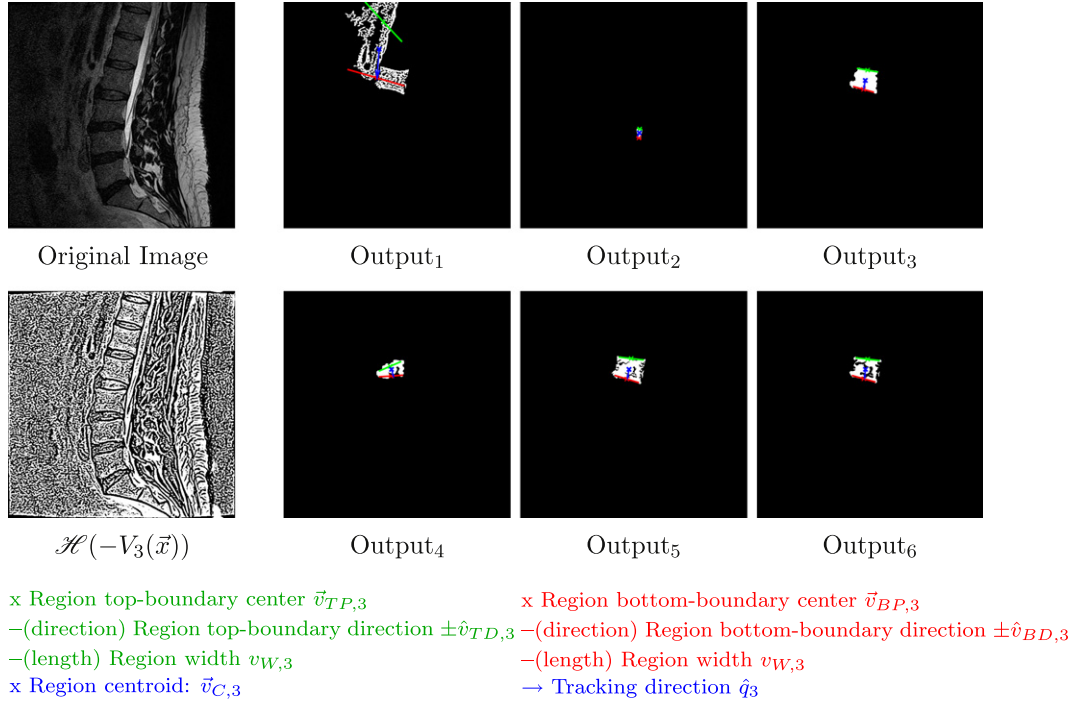


Fig. 7. An example of extracting a vertebral body (the third vertebral body, which is beneath the third disc in the image). The sub-figures $Output_1 \dots Output_6$ correspond to the outputs of Algorithm 2 based on the thresholded binary image $\mathcal{H}(-V_3(\vec{x}))$.

- guide the contours to lie on the annulus outer-boundaries (the anterior and the posterior boundaries of the disc). The anterior and the posterior boundaries are expected to be aligned along the disc superior–inferior axis. From the disc region to the vicinity of the disc across these boundaries, the voxel intensity is increasing. In a small local region around these boundaries, the gradient consistency becomes significant. Based on Eq. (11), these are detected by,

$$D_{4,i}(\vec{x}; r)(\hat{d}_{L,i} \cdot (\text{Contour inward normal})), \text{ where}$$

$$D_{4,i}(\vec{x}; r) = \hat{d}_{L,i} \hat{j}_1 \hat{j}_2 (\vec{\phi} * I(\vec{x}; r)). \quad (31)$$

- include the high intensity disc-nuclei. In order to distinguish the disc-nuclei from the high intensity vertebral bodies and spinal cords, the disc-nuclei are identified as the isolated unsegmented regions of the segmentation results of the low intensity disc-annulus.

The detection radii for Eqs. (28)–(31) are determined using the strongest-over-radii strategy,

$$r_{k,i}(\vec{x}) = \arg \max_{r \in \mathbb{R}_+} |D_{k,i}(\vec{x}; r)|, k \in [1, 4]. \quad (32)$$

Fig. 9b–e visualize the resultant values of the aforementioned descriptors $D_{1,i}(\cdot)$, $D_{2,i}(\cdot)$, $D_{3,i}(\cdot)$ and $D_{4,i}(\cdot)$ based on the detection radii returned by Eq. (32). In Fig. 9b, $D_{1,i}(\cdot)$ conveys high contrast responses at the top- and bottom-boundaries of the disc. The longitudinal ligaments are identified by $D_{2,i}(\cdot)$ and $D_{3,i}(\cdot)$ (Fig. 9c and d). Meanwhile, the anterior and the posterior disc boundaries are highlighted as large positive or large negative values by $D_{4,i}(\cdot)$ (Fig. 9e). These four complementary descriptors well describe different parts of the disc boundary, or highlight the adjacent structures. Based on these descriptors, the segmentation phase is capable of segmenting the discs, despite the challenges illustrated in Fig. 1.

4.2. Level set based energy minimization

Denote \mathcal{Z} be a closed curve in a middle sagittal plane. It comprises a set of 3D coordinates representing the points along the curve on the sagittal plane. Based on the above descriptors, an energy functional for each disc is formulated to reflect the quality of a segmentation,

$$\mathcal{F}_i(\mathcal{Z}) = \int_{\mathcal{Z}} \left(-D_{1,i}(\mathcal{Z}(A); r_{1,i}(\mathcal{Z}(A))) + D_{2,i}(\mathcal{Z}(A); r_{2,i}(\mathcal{Z}(A))) \right. \\ \left. + D_{3,i}(\mathcal{Z}(A); r_{3,i}(\mathcal{Z}(A))) \right) dA \\ - \int_{\delta\mathcal{Z}} \left(D_{4,i}(\mathcal{Z}_i(B); r_{4,i}(\mathcal{Z}(B))) (\hat{d}_{L,i} \cdot \mathcal{Z}_i'(B)) + \lambda \right) dB. \quad (33)$$

where λ governs the resultant contour smoothness, A and B are the area and the length parameterization of \mathcal{Z} . This energy functional is minimized by taking the first variation and evolving a level set function (Whitaker, 1998) in a gradient descent fashion. We adapt the spatially varying curvature regularization weight (Caselles et al., 1997) in our contour evolution equation to enforce a stronger contour smoothness at positions away from the disc centers. The level set function φ_i for the i th disc is evolved over time t according to

$$\frac{\partial \varphi_i}{\partial t} \Big|_{\varphi_i=0} = \left(D_{1,i} - D_{2,i} - D_{3,i} + \frac{\partial}{\partial \hat{d}_{L,i}} \left((I * \vec{\phi}(\cdot; r_{4,i})) \cdot \hat{d}_{L,i} \right) \right. \\ \left. + g_i \lambda (\vec{\nabla} \cdot \frac{\vec{\nabla} \varphi_i}{|\vec{\nabla} \varphi_i|}) \right) |\vec{\nabla} \varphi_i|. \quad (34)$$

Here the arguments \vec{x} and t for φ_i ; \vec{x} for g_i , $D_{k,i}$ and $r_{4,i}$; $r_{1,i}$, $r_{2,i}$ and $r_{3,i}$ are omitted to simplify the notation. To achieve slice based segmentation, the derivatives of φ_i are computed only along the in-plane directions. The term $g_i(\cdot)$ is the spatially varying regularization weight,

- x Region top-boundary center $\vec{v}_{TP,i}$
- (direction) Region top-boundary direction $\pm\hat{v}_{TD,i}$
- (length) Region width $v_{W,i}$
- x Region bottom-boundary center $\vec{v}_{BP,i}$
- (direction) Region bottom-boundary direction $\pm\hat{v}_{BD,i}$
- (length) Region width $v_{W,i}$
- Resultant region of coarse vertebral body detection
- x Vertebral body centroid: $\vec{v}_{C,i}$
- Vertebra tracking direction \hat{q}_i
- x Estimated successive tracking point \vec{z}_{i+1}

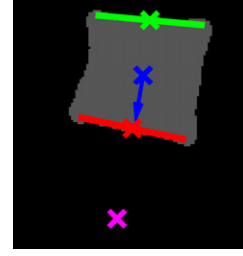
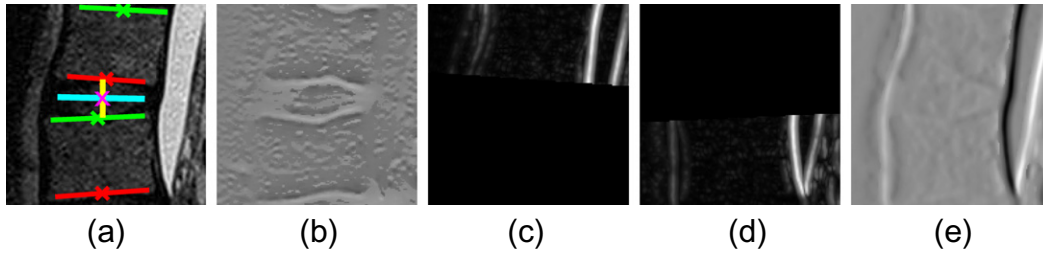


Fig. 8. A summary of the vertebra statistics being extracted from the coarse vertebral body detection result. For simplicity of discussion, $\hat{v}_{TB,i}$ and $\hat{v}_{BD,i}$ are pointing along the anterior direction (left in the sagittal slice) in this paper.



- x Vertebral region top-boundary center $\vec{v}_{TP,i}$
- (length) Vertebral region width $v_{W,i}$
- (direction) Vertebral region top-boundary direction $\pm\hat{v}_{TD,i}$
- x Vertebral region bottom-boundary center $\vec{v}_{BP,i}$
- (length) Vertebral region width $v_{W,i}$
- (direction) Vertebral region bottom-boundary direction $\pm\hat{v}_{BD,i}$
- Preliminary disc superior-inferior axis $\pm\hat{d}_{S,i}$ and preliminary disc thickness $d_{T,i}$
- Preliminary disc anterior-posterior axis $\pm\hat{d}_{L,i}$ and preliminary disc width $d_{W,i}$

Fig. 9. (a) A summary of the preliminary disc statistics, along with the statistics of the adjacent vertebrae. For simplicity of discussion, $\hat{d}_{L,i}$ and $\hat{d}_{S,i}$ are pointing along the anterior direction (left in sagittal slices) and the bottom direction respectively in this study. (b–e) The resultant values of the descriptors $D_{1,i}(\cdot)$, $D_{2,i}(\cdot)$, $D_{3,i}(\cdot)$ and $D_{4,i}(\cdot)$ (Eqs. (28)–(31)). The black pixels in the sub-figures b–e represent the values of -78 , 0 , 0 and -204 respectively; the white pixels in the sub-figures b–e represent the values of 78 , 372 , 372 and 162 respectively.

$$g_i(\vec{x}) = \sqrt{\left(\frac{(\vec{x} - \vec{d}_{P,i}) \cdot \hat{d}_{S,i}}{d_{T,i}}\right)^2 + \left(\frac{(\vec{x} - \vec{d}_{P,i}) \cdot \hat{d}_{L,i}}{d_{W,i}}\right)^2}. \quad (35)$$

The initial contour is an ellipse where $g_i(\cdot) = 1$ (see the yellow ellipses in Fig. 4e). The value of $g_i(\cdot)$ soars at the positions away from the preliminary disc center. This helps restrain the evolving contour from overshooting the disc boundary if structures outside the spine nullify the boundary intensity contrast (see an example in Fig. 1b). To demonstrate the contribution of various descriptors $D_{k,i}(\cdot)$ in the final segmentation result, the manual segmentation result and the level set segmentation result are overlaid on the descriptor responses in Fig. 10.

The level set evolution is implemented using the publicly available ITK library (Ibanez et al., 2003). The parameters required to solve the differential equation (Eq. (34)) follows the description in Whitaker (1998). The evolution is terminated when the per-pixel update accumulated over 10 iterations is less than 10^{-5} . Finally, connectivity analysis is performed to the evolution result of Eq. (34) to recover the isolated unsegmented regions associated with the possibly existing high intensity disc-nuclei.

5. System summary

The anisotropic oriented flux filtering responses $[\hat{j}_1 \hat{j}_2](\psi * I(\vec{x}; r))$, $[\hat{j}_1 \hat{j}_2]^T$, $[\hat{j}_1 \hat{j}_2](\psi_{\sigma_j=2s, \sigma_a=3s} * I(\vec{x}; r))$, $[\hat{j}_1 \hat{j}_2]^T$ and $[\hat{j}_1 \hat{j}_2](\bar{\psi} * I(\vec{x}; r))$, $r \in \mathbb{R}_h$ are pre-computed offline using the fast Fourier Transform technique based on Eq. (12). They are retrieved for evaluating

various descriptors utilized in the system, Eqs. (15), (16), (18)–(21), (28)–(32) and (34). The system makes use of two manually selected positions to indicate the vertebra beneath the first target disc, and the vertebra beneath the last target disc. The selected positions are valid inside the entire corresponding vertebral bodies. This allows the same in-plane coordinates of the selected positions to be utilized in other slices of the same sequence. It further reduces the manual interaction required.

Subsequent to this minimal manual initialization, the system automatically estimates the necessary information to track the vertebral bodies, and segment the intervertebral discs in the target slices. Fig. 11 presents an overview and the work flow of the system. Readers are referred to Fig. 4a–e for the examples of the intermediate outputs of the system and the final segmentation results. To the best of our knowledge, no existing algorithm is capable of performing slice based intervertebral disc segmentation using only two manually hinted positions as the algorithm initial input. This slice based assessment follows one of the disc diagnosis standards, where only the middle sagittal slices of a volumetric scan are visually assessed. It is worth mentioning that the dynamics of the active contour described in Section 4.2 allows the contour to expand and shrink during evolution. The segmentation algorithm is therefore robust against misaligned initial contours which overshoot the disc boundaries (see the bottom disc in Fig. 4e). This is beneficial when the coarse detection of the vertebral region does not precisely locate the vertebral body's superior and inferior boundaries in the first phase of this system.

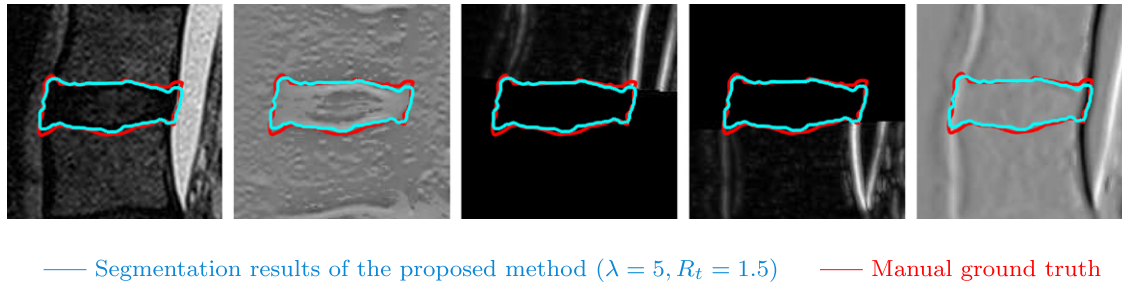


Fig. 10. The manual segmentation result and the system segmentation result, along with original image, $D_{1,i}(\cdot)$, $D_{2,i}(\cdot)$, $D_{3,i}(\cdot)$ and $D_{4,i}(\cdot)$ as shown in Fig. 9a–e.

6. Experiment

We used 22 T2- and 11 PD-MR sagittal image sequences captured from 22 distinct subjects.¹ These 22 subjects were comprised of 8 males and 14 females. Their age ranges from 31 to 85 years old (on average 55.18 years old). The patient data is provided by St. Joseph's Hospital London, Ontario, Canada and Victoria Hospital London, Ontario, Canada. The experiment employs only the middle slices where the spinal cord, the intervertebral discs and the associated vertebral bodies are visible while the vertebral pedicles are not visible. Depending on the across-plane image resolutions, the spine postures and the spine curvatures, the number of middle slices contributed by each image sequence varies from 1 to 4. There are in total 69 MR image slices, in which there are 455 discs for evaluation. The in-plane pixel sizes and plane-spacings of the sequences range from $0.41 \times 0.41 \text{ mm}^2$ to $0.86 \times 0.86 \text{ mm}^2$ and from 0.86 mm to 5 mm respectively, as shown in Table 2. For each sequence, two positions were manually selected to indicate the vertebrae underneath the first and the last target discs. The same in-plane positions of the selected position pairs were utilized for the slices extracted from the same sequence. The discussion of experimental results begins with qualitative segmentation examples, followed by quantitative results. The quantitative results concern the performance of coarse vertebral body detection and disc segmentation accuracies based on different model parameters. Using the optimal model parameters, detailed pathology-dependent disc segmentation accuracies are shown.

In Fig. 12a–e, five examples of the segmentation results of the proposed method along with the manual ground truth are shown. The great overlaps between the red curves and the blue curves demonstrates the promising segmentation accuracy of the proposed method. In the second last disc of Fig. 12b, the contour is able to halt over the ambiguous boundary at the bottom-left corner of the disc. This is because the active contour is designed to stop when the local gradient consistency is strong to capture the low contrast disc annulus outer-boundary. In addition, the spatially varying curvature regularization $g_i(\cdot)$ helps avoid the evolving contour from leaking through the ambiguous boundary. In the second disc of Fig. 12c, despite of the minor discrepancy between the proposed method result and the manual segmentation in the herniated portion of the disc, the proposed method is capable of handling disc shape variation when disc herniation occurs. This is also reflected in the accurate segmentation of the degenerated disc (the third disc in Fig. 12d). On the other hand, it nicely segments the discs associated with an abnormally deformed vertebra (the first two discs in Fig. 12e).

Among these results (Fig. 12a–e), the measures $D_{2,n}(\cdot)$, $D_{3,n}(\cdot)$ and the spatially varying curvature regularization $g_i(\cdot)$ jointly con-

fine the contour to evolving into the ligaments which have the same intensity as the disc annulus. Finally, the connectivity analysis performed on the contour evolution results allowed the entire discs to be properly segmented regardless of the visibility of the disc nuclei (Fig. 12a and d against Fig. 12b, c and e).

One cervical and upper thoracic spine (Fig. 13) which contributes two T2 midsagittal MR images is included in our dataset. It aims at visualizing the proposed system performance when handling discs which are significantly smaller than those in the lower thoracic and lumbar spines. The disc thickness of the cervical spine in this case is approximately 2.5 mm (as compared to about 3 mm to 6 mm for the lumbar discs in our database). As hinted in Section 2, the value of R_t is suggested to be half of the thickness of the thinnest detectable disc. The system favors a small value of R_t to give a better segmentation result for the small cervical and upper thoracic discs. Nonetheless, the system is able to deliver satisfactory segmentation results in most of the discs in this case for various values of R_t .

Although locating vertebral body centroids is not the focus of this study, the accuracy of centroid localization reflects the reliability of the coarse vertebral body detection procedure, which provides all necessary information for the subsequent disc segmentation phase. Table 3 presents the accuracies of the detected vertebral body centroids and the tracking points. The proposed system attains the minimum error 1.2294 mm at $R_t = 1.5$. This error is insignificant as compared to typical lumbar and upper thoracic vertebral body dimensions (approximately 30 mm high and 40 mm wide). This implies that the coarse vertebral body detection can satisfactorily locate the vertebral bodies. This is vital for the subsequent disc segmentation process. Different from the estimated vertebral body centroids which reflect the quality of the tracking procedure, the estimated tracking points are merely employed to identify the currently tracked vertebral bodies (Section 3.2). A tracking point is regarded as valid if it is located inside the correct vertebral body (see Fig. 4d as an example). Thus, the system is capable of tolerating large discrepancies between the tracking point and the actual vertebral body centroid (Table 3, the third column). This observation also illustrates the robustness of the system with the two manually selected positions, which are utilized to identify the first and the last vertebral bodies, in order to initiate and terminate the tracking procedure respectively. Analogous to the tracking points, these two positions are valid if they are located inside the target vertebral bodies. Therefore, the results shown in the third column of Table 3 suggest a large circular region (e.g. with a 13.44mm radius for $R_t = 1.5$) centered at the vertebral body centroids, where the manually selected positions are well accepted by the proposed segmentation system.

The Dice Similarity Coefficient (DSC) (Zijdenbos et al., 1994), Root Mean Squared Error (RMSE) and Mean Signed Distance Error (MSDE) between the manual ground truth and proposed method segmentation results are studied for quantitative evaluation. Denote \mathcal{Q} and

¹ The University of Western Ontario Research Ethics Board for Health Sciences Research Involving Human Subjects (HSREB) has granted approval to this study regarding the use of the clinical cases.

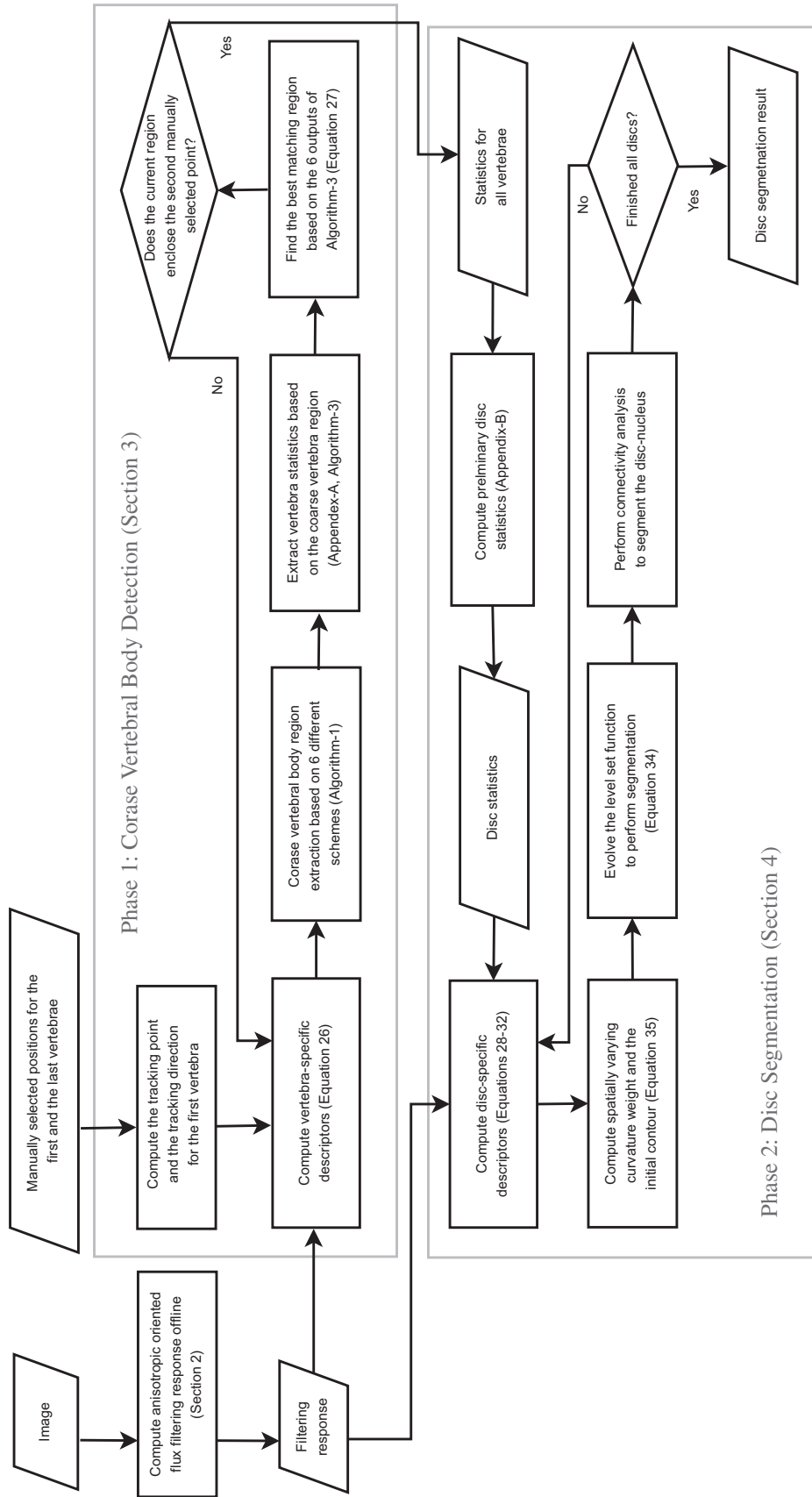


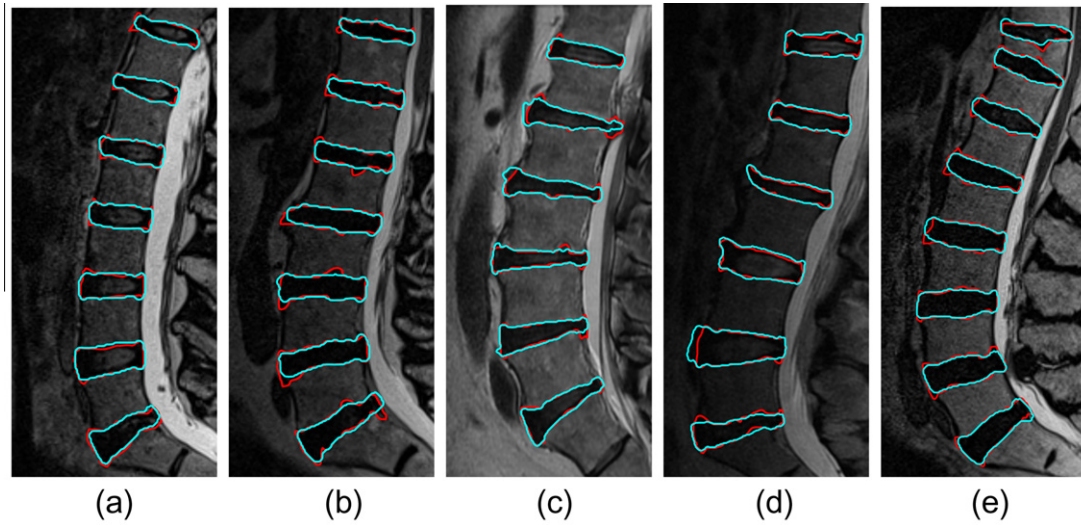
Fig. 11. The flowchart of the proposed disc segmentation system.

Table 2

The summary of the MR images used in the experiment.

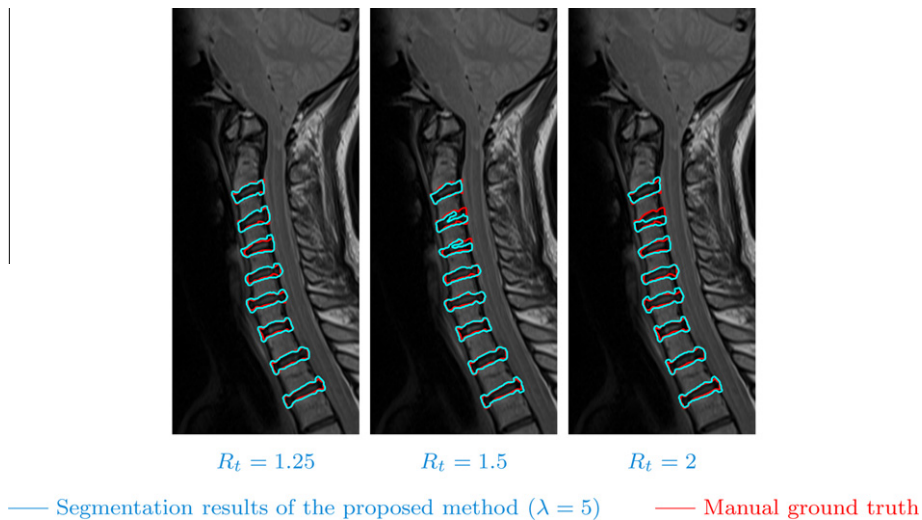
Modality	Number of sequences	In-plane pixel spacing	Slice spacing	Slice thickness	Slice dimension	Imaging Device ^a
PD-MR	10	$0.6473 \times 0.6473 \text{ mm}^2$	4.400 mm	4.000 mm	448×448 pixels	Siemens
PD-MR	1	$0.5664 \times 0.5664 \text{ mm}^2$	4.400 mm	4.000 mm	448×448 pixels	Siemens
T2-MR	1	$0.5469 \times 0.5469 \text{ mm}^2$	5.000 mm	4.000 mm	512×512 pixels	GE
T2-MR	2	$0.5859 \times 0.5859 \text{ mm}^2$	5.000 mm	4.000 mm	512×512 pixels	GE
T2-MR	1	$0.6250 \times 0.6250 \text{ mm}^2$	3.300 mm	3.000 mm	448×448 pixels	Siemens
T2-MR	3	$0.4063 \times 0.4063 \text{ mm}^2$	0.900 mm	0.900 mm	640×640 pixels	Siemens
T2-MR	1	$0.4063 \times 0.4063 \text{ mm}^2$	0.900 mm	0.900 mm	448×448 pixels	Siemens
T2-MR	3	$0.8594 \times 0.8594 \text{ mm}^2$	0.900 mm	0.900 mm	320×320 pixels	Siemens
T2-MR	6	$0.4375 \times 0.4375 \text{ mm}^2$	0.900 mm	0.900 mm	640×640 pixels	Siemens
T2-MR	3	$0.8594 \times 0.8594 \text{ mm}^2$	0.880 mm	0.880 mm	320×320 pixels	Siemens
T2-MR	1	$0.5469 \times 0.5469 \text{ mm}^2$	0.800 mm	1.600 mm	512×512 pixels	Siemens
T2-MR	1	$0.4688 \times 0.4688 \text{ mm}^2$	0.800 mm	1.600 mm	512×512 pixels	GE

^a In the 7th column of Table 2, the terms “Siemens” and “GE” correspond to the imaging devices “Magnetom Avanto 1.5T, Siemens Medical Solutions, Erlangen, Germany” and “Signa HDxt 1.5T, GE, Milwaukee, Wisconsin, USA” respectively.



— Segmentation results of the proposed method ($\lambda = 5, R_t = 1.5$) — Manual ground truth

Fig. 12. (a) A typical lower thoracic and lumbar spine. (b) A spine with a closely applied abdominal vessel, the second last disc has an ambiguous boundary and is also shown in Fig. 1b. (c) The second disc (also shown in Fig. 1c) of the spine is a herniated and degenerated disc. (d) The third disc (also shown as the first disc in Fig. 1d) is a degenerated disc. (e) A spine with an abnormally deformed vertebra (the first three discs are also shown in Fig. 1e).



— Segmentation results of the proposed method ($\lambda = 5$) — Manual ground truth

Fig. 13. The segmentation results of a cervical and upper thoracic spine using different values of R_t

Table 3

Quantitative evaluation of the vertebral body tracking point and the vertebral body centroid accuracies. $\bar{v}_{C,i}^M$ is the manual ground truth centroid of a vertebral body.

R_t	Vertebral body centroid $ \bar{v}_{C,i}^M - \bar{v}_{C,i} $	Vertebra tracking point $ \bar{v}_{C,i}^M - \bar{z}_i $
1.25	4.2859	15.6249
1.5	1.2294	13.4369
1.75	1.3815	13.5528
2	1.3078	13.7815
2.25	2.2892	14.0772
2.5	3.9910	15.8622
2.75	6.8798	18.0642

\mathcal{M} are the regions of the proposed method segmentation result and manual ground truth of an image,

$$DSC = \frac{2|\mathcal{Q} \cap \mathcal{M}|}{|\mathcal{Q}| + |\mathcal{M}|}. \quad (36)$$

DSC measures the similarity between \mathcal{Q} and \mathcal{M} . It ranges from 0 to 1, where the DSC values of 0 and 1 respectively represent no overlap and complete overlap between \mathcal{Q} and \mathcal{M} (Zijdenbos et al., 1994). Meanwhile, RMSE and MSDE quantify the averaged distance between the boundary points on $\delta\mathcal{Q}$ and those on $\delta\mathcal{M}$,

$$RMSE = \sqrt{\frac{\sum_{\bar{q} \in \delta\mathcal{Q}} (\min_{\bar{m} \in \delta\mathcal{M}} |\bar{q} - \bar{m}|^2) + \sum_{\bar{m} \in \delta\mathcal{M}} (\min_{\bar{q} \in \delta\mathcal{Q}} |\bar{q} - \bar{m}|^2)}{\sum_{\bar{q} \in \delta\mathcal{Q}} 1 + \sum_{\bar{m} \in \delta\mathcal{M}} 1}}, \quad (37)$$

$$MSDE = \frac{\sum_{\bar{q} \in \delta\mathcal{Q}} (\text{sgn}(\bar{q}) \min_{\bar{m} \in \delta\mathcal{M}} |\bar{q} - \bar{m}|) + \sum_{\bar{m} \in \delta\mathcal{M}} (\text{sgn}(\arg \min_{\bar{q} \in \delta\mathcal{Q}} |\bar{q} - \bar{m}|) \min_{\bar{q} \in \delta\mathcal{Q}} |\bar{q} - \bar{m}|)}{\sum_{\bar{q} \in \delta\mathcal{Q}} 1 + \sum_{\bar{m} \in \delta\mathcal{M}} 1}}, \quad (38)$$

where four samples are drawn for one unit pixel-length and $\text{sgn}(\bar{q})$ is -1 when \bar{q} is inside \mathcal{M} , $\text{sgn}(\bar{q}) = 1$ otherwise. Zero RMSE and MSDE reflect a perfect match between \mathcal{Q} and \mathcal{M} . Negative and positive values of MSDE represent under-segmentation and over-segmentation respectively, that illustrate the segmentation bias of the proposed method.

The means and the standard deviations of DSC, RMSE and MSDE are presented in Tables 4–6 based on different parameter settings of λ and R_t . The proposed method generally yields more under-segmentation errors if the value of λ surges (Table 6). When $\lambda = 5$ and $R_t = 1.5$, the proposed method yields the most accurate segmentation with the highest mean DSC of 0.92 and the lowest mean RMSE of 0.98 mm. When λ and R_t are within the ranges of [2,10] and [1.5,2.5], in the entries inside the middle frames of Tables 4 and 5, the discrepancies between each pair of adjacent DSC-mean values or that of RMSE-mean values are smaller than the associated standard deviations. The disc segmentation results are shown to be stable and accurate over a large range of the parameter values. Beyond this stable parameter settings, occasional contour leakages occur. Leakages lower the mean values and boost the standard deviations of DSC and RMSE.

At the optimal parameter setting ($R_t = 1.5$ and $\lambda = 5$), the detailed pathology-dependent² segmentation results are shown in Table 7. In which, the mean values of RMSE, DSC and MSDE of the Groups-Normal, I, II and I&II remain within the 1 standard deviation interval of the corresponding values of the overall segmentation accuracies (Group-All). There is no significant change

in performance among different patient groups. It is because the proposed method performs detection merely based on intensity changes. Its performance is steady when handling various abnormalities if observable intensity discontinuities across the disc boundaries exist.

This experiment also illustrates the robustness of the proposed segmentation system which is examined using different MRI sequences (T2 MR and PD MR), dissimilar image resolutions (Table 2) and various spine anatomical location (from cervical spine to thoracic spine, see Fig. 13, and from thoracic spine to lumbar spine, see Fig. 12a-e), based on the validation using a large set of parameter values.

7. Conclusion and perspective

This study proposes an unsupervised intervertebral disc segmentation system based on spinal sagittal T2 and PD MR slices. The system overcomes the difficulties incurred by the intensity resemblance between discs and their adjacent structures, ambiguous disc boundaries, shape and intensity variation of discs. The segmentation system makes use of the proposed novel anisotropic oriented flux to supply low level image features for detection. Based on these low level features, various image descriptors are formulated for the detection of vertebral body regions and the disc boundaries. The segmentation framework formulated based on anisotropic oriented flux consistently delivers accurate segmentation results in the images acquired using different MRI sequences and spatial resolutions which gives a wide range of parameter values. The proposed system utilizes minimal user interaction, making it practical for clinical use.

Due to the limitation of T2 and PD MR imaging techniques, it is impractical to precisely distinguish cartilaginous disc-annuli from the attached longitudinal ligaments at the posterior and anterior sides of the discs. Thus, the disc segmentation results include small portions of the posterior and anterior ligaments. Nonetheless, the intermediate vertebra statistics, the tracked vertebral bodies and segmented disc contours offer valuable information to facilitate various clinical procedures, such as quantitative temporal analysis and post-treatment analysis, surgical planning and diagnosis. This information includes vertebral body height and labels (Roberts et al., 2005; Štern et al., 2010), disc labels (Weiss et al., 2006; Schmidt et al., 2007; Corso et al., 2008), disc orientations (Abufadel et al., 2006), disc intensity and dimensions (Pfirrmann et al., 2001).

It is possible to employ the proposed anisotropic oriented flux detection for vertebral body segmentation if the strong disturbance introduced by the spinal cord can be suppressed. Although anisotropic oriented flux is formulated for spinal image analysis, they are general for processing 2D image slices extracted from volumetric images. In medical image analysis applications where image planes are acquired or synthesized to perpendicularly intersect the interested objects, such as cardiac short-axis scan analysis (Ben Ayed et al., 2009; Punithakumar et al., 2010; Sun et al., 2005), feature extraction along vessel cross-sectional planes for vessel tracking (Aylward and Bullitt, 2002; Wink et al., 2000; Krissian et al., 2000) or spine sagittal scan analysis (Michopoulou et al., 2009; Weiss et al., 2006; Roberts et al., 2005; Pfirrmann et al., 2001), image plane orientations are calibrated manually beforehand or automatically during analysis. The calibration aims at minimizing the structure discrepancy across adjacent image planes at the same in-plane position, while exaggerating the target object boundaries in the desired image planes. The proposed anisotropic oriented flux detection which exploits the across-plane structure consistency is therefore beneficial to these applications.

² The clinical cases are diagnosed by trained radiologists according to the recommendations provided by American Society of Neuroradiology

Table 4Quantitative result evaluation, DSC (Zijdenbos et al., 1994) (Mean \pm Standard deviation) of the proposed segmentation system using different combinations of parameters.

R_t	λ				
	1	2	5	10	20
1.25	0.8956 \pm 0.1193	0.8981 \pm 0.1195	0.9033 \pm 0.1183	0.8974 \pm 0.1200	0.8795 \pm 0.1260
1.5	0.9117 \pm 0.0278	0.9149 \pm 0.0287	0.9204 \pm 0.0175	0.9171 \pm 0.0239	0.8990 \pm 0.0533
1.75	0.9076 \pm 0.0374	\pm 0.9115 \pm 0.0367	0.9150 \pm 0.0355	0.9122 \pm 0.0396	0.8922 \pm 0.0632
2	\pm 0.9093 \pm 0.0255	0.9134 \pm 0.0223	0.9184 \pm 0.0186	0.9154 \pm 0.0248	0.89480.0510
2.25	0.9031 \pm 0.0480	\pm 0.9069 \pm 0.0468	0.9119 \pm 0.0484	0.9082 \pm 0.0497	0.8918 \pm 0.0573
2.5	0.8949 \pm 0.0631	0.9010 \pm 0.0637	0.9057 \pm 0.0644	0.9023 \pm 0.0653	0.8848 \pm 0.0748
2.75	0.8798 \pm 0.1193	0.8831 \pm 0.1227	0.8965 \pm 0.1212	0.8833 \pm 0.1332	0.8636 \pm 0.1369

Table 5Quantitative result evaluation, RMSE (Mean \pm Standard deviation, in mm) of the proposed segmentation system using different combinations of parameters. The RMSE standard deviation shown in this table does not imply that the RMSE is normally distributed. In contrast to DSC and MSDE, the non-negative RMSE associated with large standard deviation and small mean values is not a normal distribution. The standard deviation is shown for illustrating the fluctuation of RMSE observed from different samples. It does not imply that RMSE is normally distributed.

R_t	λ				
	1	2	5	10	20
1.25	2.1475 \pm 5.9814	2.0272 \pm 5.9692	1.9035 \pm 6.0518	1.9300 \pm 5.5583	2.2191 \pm 5.2373
1.5	1.4389 \pm 1.3932	1.2907 \pm 1.3845	0.9829 \pm 0.3082	1.0384 \pm 0.4271	1.3676 \pm 0.9001
1.75	1.4707 \pm 1.4312	1.3301 \pm 1.4043	1.1746 \pm 1.3920	1.2129 \pm 1.1460	1.5923 \pm 1.6220
2	1.4107 \pm 0.8018	1.2105 \pm 0.5637	1.0135 \pm 0.2907	1.0737 \pm 0.4216	1.4320 \pm 0.9368
2.25	1.5106 \pm 1.1297	1.3659 \pm 1.0033	1.1297 \pm 0.7983	1.1864 \pm 0.6515	1.5028 \pm 0.9759
2.5	1.6510 \pm 1.3190	1.4824 \pm 1.1985	1.4921 \pm 2.2281	1.5360 \pm 2.1565	1.8586 \pm 2.2525
2.75	2.1226 \pm 3.5128	1.8196 \pm 2.6357	1.8181 \pm 4.3918	2.0730 \pm 4.9260	3.1155 \pm 9.6837

Table 6Quantitative result evaluation, MSDE (Mean \pm Standard deviation, in mm) of the proposed segmentation system using different combinations of parameters.

R_t	λ				
	1	2	5	10	20
1.25	-1.5147 \pm 8.7532	-1.5076 \pm 8.6139	-1.5019 \pm 8.4121	-1.9333 \pm 8.9974	-1.8982 \pm 8.2379
	-19.0211 \pm 15.9917	-18.7354 \pm 15.7202	-18.3261 \pm 15.3223	-19.9281 \pm 16.0615	-18.3740 \pm 14.5776
1.5	0.09592.0002	-0.03041.8623	-0.05791.0204	-0.15251.0467	-0.3327 1.3686
	-3.9045 \pm 4.0963	-3.7550 \pm 3.6942	-2.0987 \pm 1.9829	-2.2459 \pm 1.9409	-3.0699 \pm 2.4045
1.75	0.02422.1124	-0.0668 2.0075	-0.1387 1.8715	-0.2336 1.8604	-0.3977 1.9247
	-4.2490 \pm 4.2006	-4.0818 \pm 3.9482	-3.8817 \pm 3.6043	-3.9544 \pm 3.4872	-4.2471 \pm 3.4517
2	0.0856 1.5515	0.0424 1.3110	-0.0365 1.0658	-0.1386 1.0945	-0.3298 1.4562
	-3.0174 \pm 3.1886	-2.5796 \pm 2.6644	-2.1681 \pm 2.0951	-2.3276 \pm 2.0504	-3.2422 \pm 2.5826
2.25	0.2579 2.3338	0.2134 2.1779	0.1391 1.9774	-0.0994 1.6339	-0.3002 1.6337
	-4.4097 \pm 4.9255	-4.1424 \pm 4.5692	-3.8157 \pm 4.0939	-3.3672 \pm 3.1684	-3.5676 \pm 2.9672
2.5	0.3243 2.5579	0.2685 2.3605	0.1470 2.6364	-0.0763 2.3878	-0.3465 2.4577
	-4.7915 \pm 5.4401	-4.4525 \pm 4.9895	-5.1258 \pm 5.4198	-4.8519 \pm 4.6993	-5.2619 \pm 4.5689
2.75	0.1255 3.9258	0.1351 3.0466	-0.0285 3.9916	-0.5343 4.5288	-1.0543 8.0997
	-7.7261 \pm 7.9771	-5.9581 \pm 6.2283	-8.0117 \pm 7.9547	-9.5919 \pm 8.5233	-17.2537 \pm 15.1451

Table 7Pathology-dependent quantitative segmentation result of the proposed method, based on $R_t = 1.5$, $\lambda = 5$. Group-I represents degenerated discs. Group-II represents discs which involve any one of the followings: extrusion, herniation, protrusion and bulging, that affects the central or paracentral regions of the respective disc. Group-All repeats the results shown in Tables 4–6 for $R_t = 1.5$, $\lambda = 5$.

Patient group	Normal	I	II	I & II	All
RMSE					
Mean	0.7761	1.1686	1.0359	1.0278	0.9829
DSC					
Mean	0.9179	0.9088	0.9235	0.9145	0.9204
SD	0.0366	0.0357	0.0160	0.0342	0.0175
95% Confidence interval	[0.8447, 0.9911]	[0.8374, 0.9802]	[0.8915, 0.9555]	[0.8461, 0.9829]	[0.8854, 0.9554]
MSDE					
Mean	0.1597	-0.1904	-0.0984	-0.1663	-0.0579
SD	0.7595	1.1529	1.0312	1.0412	1.0204
95% Confidence interval	[-1.3593, 1.6787]	[-2.4962, 2.1154]	[-2.1608, 1.9640]	[-2.2487, 1.9161]	[-2.0987, 1.9829]
Number of discs	110	109	310	74	455

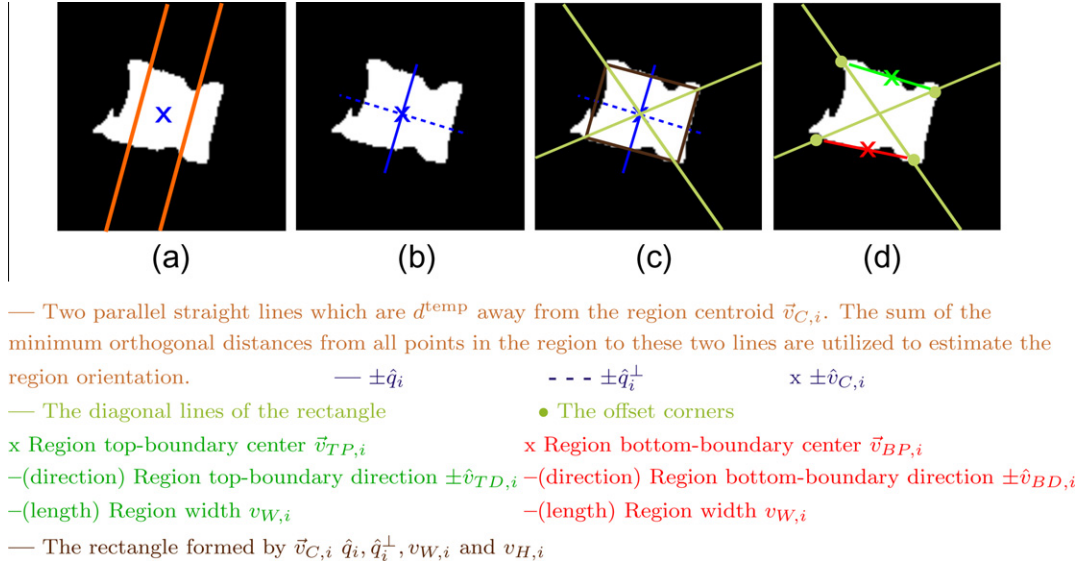


Fig. 14. (a) Finding the object orientation. (b) Partitioning the object into four quadrants. (c) Finding the diagonal lines, where each quadrant has one corresponding diagonal line. (d) Offset the corners along the diagonal lines and retrieve the region top- and bottom-boundary statistics.

Acknowledgement

This work was supported by the Mitacs-Accelerate fellowship (App. Ref. IT00716) granted to the first author of this paper.

Appendix A. Vertebra statistics

Based on the coarse detection of vertebral body results described in Algorithm 2, the vertebra statistics are obtained by approximating the detected region as a quadrangle. This procedure involves three steps. The first step begins by finding the region centroid and the average point distance to the centroid (lines 1–2 of Algorithm 3). The sum of the minimum perpendicular distance from every pixel to two parallel lines which are double of the aforementioned average distance apart is computed (Fig. 14a). The directions that gives the minimal summed distance, or their perpendicular directions are selected as the object direction (lines 3–10 of Algorithm 3, Fig. 14b). In the second step, the region width and the region height are retrieved (lines 11–12 of Algorithm 3). Based on the region centroid, direction, width and the region height, the detected region can be treated as a rectangle. In the final step, each corner of this rectangle is offset along the associated diagonal line (Fig. 14c) based on the distance between the centroid and the pixels which are farthest away from the centroid in the corresponding quadrant (lines 14–18 of Algorithm 3). The region top- and bottom-boundaries are acquired based on the region top- and bottom-corners respectively (line 19 of Algorithm 3, Fig. 14d).

Appendix B. Preliminary estimation of disc positions, sizes and orientations

The preliminary disc positions, sizes and orientations are captured as centroid $\hat{d}_{p,n}$, preliminary thickness $d_{T,n}$, superior–inferior axis $\hat{d}_{S,n}$, width $d_{W,n}$, anterior–posterior axis $\hat{d}_{L,n}$ (Fig. 9a). This information are computed based on the adjacent vertebral body

top- and bottom-boundaries. Suppose there are N vertebral bodies being tracked, for the first disc in the image,

$$\begin{aligned} & \bullet \hat{d}_{T,1} = \min d_{T,i}; \\ & \bullet \hat{d}_{p,1} = \frac{i_0^{(2\dots N)}}{\hat{v}_{TP,1}} - d_{T,1}\hat{q}_0; \\ & \bullet \hat{d}_{W,1} = v_{W,1}; \\ & \bullet \hat{d}_{L,1} = \hat{v}_{TD,1} \begin{bmatrix} 0 & 1 \\ -1 & 0 \end{bmatrix} \begin{bmatrix} \hat{j}_1 \\ \hat{j}_2 \end{bmatrix} \hat{d}_{L,1}. \\ & \bullet \hat{d}_{S,1} = \begin{bmatrix} \hat{j}_1 & \hat{j}_2 \end{bmatrix} \begin{bmatrix} 0 & 1 \\ -1 & 0 \end{bmatrix} \begin{bmatrix} \hat{j}_1 \\ \hat{j}_2 \end{bmatrix} \hat{d}_{L,1}. \end{aligned}$$

For the rest of the discs ($i > 1$),

$$\begin{aligned} & \bullet \hat{d}_{T,i} = |\vec{v}_{TP,i} - \vec{v}_{BP,i-1}|; \\ & \bullet \hat{d}_{p,i} = \frac{\hat{v}_{BP,i-1} + \hat{v}_{TP,i}}{2}; \\ & \bullet \hat{d}_{W,i} = \frac{v_{W,i} + v_{W,i-1}}{2}; \\ & \bullet \hat{d}_{L,i} = \frac{\hat{v}_{TD,i} + \hat{v}_{BD,i-1}}{2} \begin{bmatrix} 0 & 1 \\ -1 & 0 \end{bmatrix} \begin{bmatrix} \hat{j}_1 \\ \hat{j}_2 \end{bmatrix} \hat{d}_{L,i}. \\ & \bullet \hat{d}_{S,i} = \begin{bmatrix} \hat{j}_1 & \hat{j}_2 \end{bmatrix} \begin{bmatrix} 0 & 1 \\ -1 & 0 \end{bmatrix} \begin{bmatrix} \hat{j}_1 \\ \hat{j}_2 \end{bmatrix} \hat{d}_{L,i}. \end{aligned}$$

Algorithm 2. CoraseVertebraExtraction

Perform coarse extraction of the vertebral body region using four variants of the conventional morphology based scheme

Input: A binary image $B(\cdot)$ and position vector \vec{y}

Output: Three binary images denoted as Output_m,

$m \in \{1 \dots 6\}$. They have a value 1 in the extracted regions, 0 in the background.

RegionExtraction₁[$B(\cdot), \vec{y}$]

1: Output₁ := ConnectedTo[$B(\cdot), \vec{y}$]

2: Output₂ := $\mathcal{H}\mathcal{D}\{\text{ConnectedTo}[\mathcal{H}(\mathcal{D}\{B(\cdot)\} - R_t), \vec{y}]\} + R_t$

3: $B^{\text{filled}}(\cdot) := B(\cdot)$

4: In $B^{\text{filled}}(\cdot)$, search the isolated background component of $B(\cdot)$, fill 1 to the components whose maximum widths are less than R_t

5: Output₃

:= $\mathcal{H}\mathcal{D}\{\text{ConnectedTo}[\mathcal{H}(\mathcal{D}\{B^{\text{filled}}(\cdot)\} - R_t), \vec{y}]\} + R_t$

6: $B^{\text{filled-2}}(\cdot) := B(\cdot)$

- 7: In $B^{\text{filled-2}}(\cdot)$, fill the isolated background regions having areas smaller than πR_t^2
 - 8: **Output**₄
 $:= \mathcal{H}(\mathcal{D}\{\text{ConnectedTo}[\mathcal{H}(\mathcal{D}\{B^{\text{filled-2}}(\cdot)\} - R_t), \vec{y}]\} + R_t)$
 - 9: $B^{\text{MDDT}}(\cdot) := \mathcal{H}(\mathcal{D}^{\text{max}}\{\mathcal{H}(\mathcal{D}\{B(\cdot)\} - R_t)\} + 2R_t)$
 - 10: $B^{\text{MDDT-filled}}(\cdot) := \mathcal{H}(B^{\text{MDDT}}(\cdot) + B(\cdot))$
 - 11: **Output**₅ $:= \text{ConnectedTo}[B^{\text{MDDT-filled}}(\cdot), \vec{y}]$
 - 12: $B^{\text{temp}}(\cdot) := B^{\text{MDDT-filled}}(\cdot)$
 - 13: In $B^{\text{temp}}(\cdot)$, fill the isolated background regions having areas smaller than πR_t^2
 - 14: **Output**₆ $:= \text{ConnectedTo}[\mathcal{H}(\mathcal{D}^{\text{max}}\{B^{\text{temp}}(\cdot)\} - R_t), \vec{y}]$
- END

Algorithm 3. VertebraStatistic

- Extract directional and positional information of the i th vertebral body
- Input:** A binary image $B(\cdot)$
- Output:** $\vec{v}_{C,i}$, $v_{H,i}$, $v_{W,i}$, \hat{q}_i , $\vec{v}_{TP,i}$, $\vec{v}_{TD,i}$, $\vec{v}_{BP,i}$ and $\vec{v}_{BD,i}$ (see Fig. 4b for these variables)
- VertebraStatistic[$B(\cdot)$]
- 1: $\vec{v}_{C,i} := \text{Mean}(\vec{y})$,
 $\forall \vec{y} : B(\vec{y}) = 1$
 - 2: $d^{\text{temp}} := \text{Mean}(|\vec{y} - \vec{v}_{C,i}|)$
 - 3: $\hat{q}^{\text{temp}} := \arg \max_{\hat{q}} (\min_{\hat{\omega}} |\vec{y} \cdot \hat{\omega} - d^{\text{temp}}|, |\vec{y} \cdot \hat{\omega} + d^{\text{temp}}|), \forall \vec{y} : B(\vec{y}) = 1$ (see Fig. 14a)
 - 4: Define $\hat{q}^{\text{temp}\perp}$, where $\hat{q}^{\text{temp}\perp} \cdot \hat{q}^{\text{temp}} = 0$
 - 5: **if** ($i > 1$) **then**
 - 6: $\hat{q}_i := \arg \max_{\hat{q} \in \{\hat{q}^{\text{temp}\perp}, -\hat{q}^{\text{temp}\perp}\}} (\hat{q}^{\text{temp}}, -\hat{q}^{\text{temp}}) \cdot (\vec{z}' - \vec{v}_{BP,i-1})$
 - 7: **else**
 - 8: $\hat{q}_i := \arg \max_{\hat{q} \in \{\hat{q}^{\text{temp}\perp}, -\hat{q}^{\text{temp}\perp}, \hat{q}^{\text{temp}}, -\hat{q}^{\text{temp}}\}} (\hat{q}^{\text{temp}\perp} \cdot (\vec{z}' - \vec{z}_1))$
 - 9: **end if**
 - 10: Define \hat{q}_i^\perp , where $\hat{q}_i^\perp \cdot \hat{q}_i = 0$ (see Fig. 14b)
 - 11: $v_{H,i} := 2\text{Mean}|\vec{y} \cdot \hat{q}_i|, \forall \vec{y} : B(\vec{y}) = 1$
 - 12: $v_{W,i} := 2\text{Mean}|\vec{y} \cdot \hat{q}_i^\perp|, \forall \vec{y} : B(\vec{y}) = 1$
 - 13: Partition the region $B(\cdot) == 1$ into four quadrants based on \hat{q}_i
 - 14: **for** each quadrant **do**
 - 15: Find the $[d^{\text{temp}}]$ pixels which are farthest away from the centroid in the current quadrant
 - 16: $d^{\text{temp-2}} = \text{Averaged distance between these } [d^{\text{temp}}] \text{ pixels to the centroid}$
 - 17: The quadrangle corner of the current quadrant is re-estimated as the location where is in the distance of $d^{\text{temp-2}}$ away from the centroid along the diagonal line associated with the current quadrant. (see Fig. 14c)
 - 18: **end for**
 - 19: $\vec{v}_{TP,i}$ and $\vec{v}_{TD,i}$ ($\vec{v}_{BP,i}$ and $\vec{v}_{BD,i}$) are the average of and the normalized relative direction of the two top-coroners (bottom-coroners) of the quadrangle respectively; without loss of generality, $\vec{v}_{TD,i}$ and $\vec{v}_{BD,i}$ are pointing from posterior to anterior
 - 20: $\vec{z}_{i+1} = \vec{v}_{C,i} + 1.5 \frac{(v_{H,i} + v_{W,i})}{2} \hat{q}_i$
- END
-

References

- Abufadel, A., Slabaugh, G., Unal, G., Zhang, L., Odry, B., 2006. Interacting active rectangles for estimation of intervertebral disk orientation. In: ICPR, pp. 1013–1016.
- Aylward, S., Bullitt, E., 2002. Initialization, noise, singularities, and scale in height ridge traversal for tubular object centerline extraction. TMI 21, 61–75.
- Ben Ayed, I., Li, S., Ross, I., 2009. Embedding overlap priors in variational left ventricle tracking. TMI 28, 1902–1913.
- Bracewell, R., 1986. The Fourier Transform and its Application. McGraw-Hill, New York.
- Caselles, V., Kimmel, R., Sapiro, G., 1997. Geodesic active contours. IJCV 22, 61–79.
- Chevretil, C., Chérier, F., Grimard, G., Aubin, C., 2007. Watershed segmentation of intervertebral disk and spinal canal from MRI images, in: ICIAR, pp. 1017–1027.
- Corso, J., Alomari, R., Chaudhary, V., 2008. Lumbar disc localization and labeling with a probabilistic model on both pixel and object features. In: MICCAI.
- Ibanez, L., Schroeder, W., Ng, L., Cates, J., 2003. The ITK Software Toolkit.
- Kadoury, S., Paragios, N., 2010. Nonlinear embedding towards articulated spine shape inference using higher-order MRFs. In: MICCAI.
- Krissian, K., Malandain, G., Ayache, N., Vaillant, R., Troussset, Y., 2000. Model-based detection of tubular structures in 3D images. Computer Vision and Image Understanding 80, 130–171.
- Law, M., Chung, A., 2008. Three dimensional curvilinear structure detection using optimally oriented flux. In: ECCV, pp. 368–382.
- Law, M., Chung, A., 2009. Efficient implementation for spherical flux computation and its application to vascular segmentation. TIP 18, 596–612.
- Law, M., Chung, A., 2010. An oriented flux symmetry based active contour model for three dimensional vessel segmentation. In: ECCV, pp. 720–734.
- Lindeberg, T., 1998. Edge detection and ridge detection with automatic scale selection. IJCV 30, 117–156.
- Lowe, D., 2004. Distinctive image features from scale-invariant keypoints. IJCV 60, 91–110.
- Manniesing, R., Viergever, M., Niessen, W., 2006. Vessel enhancing diffusion a scale space representation of vessel structures. Media 10, 815–825.
- Marr, D., Hildreth, E., 1980. Theory of edge detection. Proc. Roy. Soc. Lond. (B) 207, 187–217.
- Michopoulou, S., Costaridou, L., Panagiotopoulos, E., Speller, R., Panayiotakis, G., Todd-Pokropek, A., 2009. Atlas-based segmentation of degenerated lumbar intervertebral discs from MR images of the spine. TBE 56, 2225–2231.
- Nyul, L., Kanyo, J., Máté, E., Makay, G., Balogh, E., Fidrich, M., Kuba, A., 2005. Method for automatically segmenting the spinal cord and canal from 3D CT images. In: CAIP, p. 456.
- Okada, K., Comaniciu, D., Krishnan, A., 2004. Scale selection for anisotropic scale-space: application to volumetric tumor characterization, in: CVPR, pp. 594–601.
- Peng, Z., Zhong, J., Wee, W., Lee, J., 2005. Automated vertebra detection and segmentation from the whole spine MR image. In: EMBS, pp. 2527–2530.
- Perona, P., Malik, J., 1990. Scale-space and edge detection using anisotropic diffusion. PAMI 12, 629–639.
- Pfirrmann, C., Metzendorf, A., Zanetti, M., Hodler, J., Boos, N., 2001. Magnetic resonance classification of lumbar intervertebral disc degeneration. SPINE 26, 1873–1878.
- Punithakumar, K., Ben Ayed, I., Ross, I.G., Islam, A., Chong, J., Li, S., 2010. Detection of left ventricular motion abnormality via information measures and bayesian filtering. TITB 14, 1106–1113.
- Roberts, N., Gratin, C., Whitehouse, G., 2005. MRI analysis of lumbar intervertebral disc height in young and older populations. J. MRI 7, 880–886.
- Sato, Y., Nakajima, S., Shiraga, N., Atsumi, H., Yoshida, S., Koller, T., Gerig, G., Kikinis, R., 1998. Three-dimensional multi-scale line filter for segmentation and visualization of curvilinear structures in medical images. Media 2, 143–168.
- Schmidt, S., Kappes, J., Bergtholdt, M., Pekar, V., Dries, S., Bystrov, D., Schnörr, C., 2007. Spine detection and labeling using a parts-based graphical model. In: IPMI, pp. 122–133.
- Shi, R., Sun, D., Qiu, Z., Weiss, K., 2007. An efficient method for segmentation of MRI spine images. In: IC Comp. Med. Eng., pp. 713–717.
- Sun, W., Cetin, M., Chan, R., Reddy, V., Holmvang, G., Chandar, V., Willsky, A., 2005. Segmenting and tracking the left ventricle by learning the dynamics in cardiac images. In: IPMI, pp. 553–565.
- Vasilevskiy, A., Siddiqi, K., 2002. Flux maximizing geometric flows. PAMI 24, 1565–1578.
- Štern, D., Likar, B., Pernuš, F., Vrtovc, T., 2010. Automated detection of spinal centrelines, vertebral bodies and intervertebral discs in CT and MR images of lumbar spine. Phys. Med. Biol. 55, 247–264.
- Weiss, K., Storr, J., Banto, R., 2006. Automated spine survey iterative scan technique. Radiology 239, 255–262.
- Whitaker, R., 1998. A level-set approach to 3D reconstruction from range data. IJCV 29, 203–231.
- Wink, O., Niessen, W., Viergever, M., 2000. Fast delineation and visualization of vessels in 3-D angiographic images. TMI 19, 337–346.
- Xu, C., Prince, J., 1998. Snakes, shapes, and gradient vector flow. TIP 7, 359–369.
- Zijdenbos, A., Dawant, B., Margolin, R., Palmer, A., 1994. Morphometric analysis of white matter lesions in MR images: method and validation. TMI 13, 716–724.